



HAL
open science

First characterization of the cooling of the paleo-geothermal system of Terre-de-Haut (Les Saintes archipelago, Guadeloupe): Application of fluid inclusion and chlorite thermometry

Gildas Beauchamps, Franck Bourdelle, Michel Dubois, Ronan Hebert,
Béatrice Ledésert

► To cite this version:

Gildas Beauchamps, Franck Bourdelle, Michel Dubois, Ronan Hebert, Béatrice Ledésert. First characterization of the cooling of the paleo-geothermal system of Terre-de-Haut (Les Saintes archipelago, Guadeloupe): Application of fluid inclusion and chlorite thermometry. *Journal of Volcanology and Geothermal Research*, 2021, 419, pp.107370. 10.1016/j.jvolgeores.2021.107370 . hal-03699400

HAL Id: hal-03699400

<https://hal.science/hal-03699400v1>

Submitted on 22 Aug 2023

HAL is a multi-disciplinary open access archive for the deposit and dissemination of scientific research documents, whether they are published or not. The documents may come from teaching and research institutions in France or abroad, or from public or private research centers.

L'archive ouverte pluridisciplinaire **HAL**, est destinée au dépôt et à la diffusion de documents scientifiques de niveau recherche, publiés ou non, émanant des établissements d'enseignement et de recherche français ou étrangers, des laboratoires publics ou privés.



Distributed under a Creative Commons Attribution - NonCommercial 4.0 International License

1 **First characterization of the cooling of the paleo-geothermal system of Terre-de-Haut (Les**
2 **Saintes archipelago, Guadeloupe): application of fluid inclusion and chlorite thermometry.**

3

4 Gildas Beauchamps^a, Franck Bourdelle^b, Michel Dubois^b, Ronan Hébert^a, Béatrice Ledésert^a

5 ^aGéosciences et Environnement Cergy, CY Cergy Paris Université, 1 Rue Descartes, 95000 Neuville-
6 sur-Oise, France

7 ^b Univ. Lille, Institut Mines-Télécom, Univ. Artois, Junia, ULR 4515 - LGCgE, Laboratoire de
8 Génie Civil et géo-Environnement, F-59000 Lille, France

9

10 **Abstract**

11 Due to its geodynamic location in the Lesser Antilles arc, Basse-Terre of Guadeloupe displays an
12 active volcanism which is favourable to the development of high-enthalpy geothermal energy. An
13 exhumed analogue of the Bouillante geothermal reservoir has been recently characterized in Terre-
14 de-Haut island (Les Saintes archipelago), giving an opportunity to study the cooling of a natural
15 geothermal system and the related alterations.

16 By coupling chlorite geothermometry and primary fluid inclusions in associated zoned quartz
17 crystals located in N70 trending fractures, new insights on the Terre-de-Haut paleo-geothermal
18 evolution can be inferred by distinguishing three new different episodes during functioning and
19 cooling of this system : (i) a temperature of at least 240-270°C in fluid inclusions trapped in the
20 quartz core, (ii) chlorite formation at about 120°C, and (iii) temperatures of ~50°C - or less - in
21 fluid inclusions of the quartz outer growth zones. Fluid inclusions also reveal that the hydrothermal
22 fluid is of low salinity (2 wt% NaCl), probably of meteoric and sea water origin. Additionally, a
23 second type of fluid inclusions observed in a banded quartz vein indicates at least an episode of a
24 CO₂-(H₂O) fluid, with traces of H₂S. Hence, some similarities can be highlighted between Terre-de-
25 Haut and the Bouillante active geothermal systems in term of the highest temperatures of circulation

26 events and gas composition, despite a difference in fluid origin. This study shows that some
27 alteration episodes also occur at low temperature during the cooling of the geothermal system.
28 Moreover, the N70 trending fractures, that have been identified as drains for the hot temperature
29 fluids, have to be considered for future geothermal exploration.

30 **Keywords**

31 Hydrothermal alteration; fluid inclusion; chlorite thermometry; paleo-geothermal system; Terre-de-
32 Haut (Guadeloupe)

33

34 **1. Introduction**

35 The Lesser Antilles volcanic arc is related to a subduction zone, where the North-American plate
36 sinks under the Caribbean plate. This particular geodynamic system, with active volcanism, is
37 favourable to the formation of geothermal fields. This is the case of Basse-Terre of Guadeloupe,
38 which displays an active geothermal field named Bouillante, exploited for electric power generation
39 and producing 15 MWe (Bouchot et al., 2010).

40 Following the global trend of seeking new sources of clean and renewable energy, the GEOTREF
41 program aims to identify a geothermal resource a few kilometres south of Bouillante, at a depth
42 around 2 km. The nearby Terre-de-Haut island (Les Saintes archipelago, West Indies, France;
43 Bouysse, 1983) has long been known to host a hydrothermally altered zone (Jacques et al., 1984;
44 Jacques and Maury, 1988a, b). Recently, this altered zone was studied in more details from structural
45 and mineralogical points of view (Verati et al., 2016; Beauchamps et al., 2019), emphasizing a clay
46 mineral distribution similar to that encountered vertically in the active geothermal field of Bouillante
47 (Beauchamps et al., 2019). Indeed, the altered zone shows a clear clay mineral zonation, with chlorite
48 in the central part, illite around it and smectite in the outer rim. In fact, Terre-de-Haut corresponds to
49 an exhumed paleo-geothermal system, and can be considered as an analogue of the active system
50 located below Bouillante.

51 The aim of this study is to document the Terre-de-Haut geothermal system evolution, to compare it
52 with the still-active system of Bouillante, and to obtain information about GEOTREF's exploration
53 zone. Thanks to erosion, the Terre-de-Haut paleo-geothermal system is exhumed and shows a clear
54 2-D near horizontal insight, allowing the sampling of several newly formed minerals and
55 hydrothermally-altered rocks. Chlorite-bearing altered andesite was sampled in the "chlorite zone"
56 defined by Beauchamps et al. (2019), and neoformed quartz were especially collected in two N70
57 oriented fractures. In order to identify the major hydrothermal events of this system, two types of
58 thermometric approaches were applied: the chlorite geothermometry, using the more recent low T-
59 adapted thermometers, and fluid inclusion microthermometry, from sampled quartz.

60

61 **2. Geological Context**

62 Terre-de-Haut island belongs to the Guadeloupe archipelago and more precisely to the Les Saintes
63 sub-archipelago. It is located in the inner active arc of the Lesser Antilles arc (Bouysse, 1983; Figure
64 1A), that results from the subduction of the North American plate under the Caribbean plate at a
65 velocity of approximately 2 cm.yr^{-1} (Hawkesworth and Powell, 1980; DeMets et al., 2000; Symithe
66 et al., 2015).

67 Only few literature has long been available about the geology of Terre-de-Haut (Javey et al., 1974;
68 Jacques et al., 1984; Jacques and Maury, 1988a, b) but structural, petrographic and petrophysical data
69 were recently published (Zami et al., 2014; Verati et al., 2016; Navelot et al., 2018; Beauchamps et
70 al., 2019). Verati et al. (2016) recognise four families of fault systems, active from 3 to 2 Ma, trending,
71 from the oldest to the most recent: (1) N050-N70, (2) N130-N140, (3) N090-N110 and (4) N000-
72 N020. According to kinematic indicators and morphostructural observations these four families
73 display normal-slip movements, and three of them also a strike-slip movement (sinistral or dextral).
74 The N090-N110 trending fault system is the only one with no evidence for strike-slip movement.
75 Kinematic indicators revealing both dextral and sinistral strike-slips suggest that the N000-N020 and
76 N050-N70 systems were active and reactivated at different stages during the tectonic evolution of the

77 Les Saintes archipelago (Verati et al., 2016). These four families of fault systems are consistent with
78 the global tectonic framework of the entire Guadeloupe archipelago (Verati et al., 2016). The 2004
79 Mw 6.3 Les Saintes earthquake (Beauducel et al., 2005) was correlated with a pure normal faulting
80 with NW-SE trending nodal planes, compatible with the identified onshore N130-N140 faults. This
81 indicates that the inherited fault network is likely to be reactivated during the present-day plate
82 convergence (Verati et al., 2016).

83 The most recent geochronological data (Zami et al., 2014) revealed the presence of three main
84 subaerial volcanic phases on Terre-de-Haut (Figure 1B). The first phase, 2.98 ± 0.04 Ma old,
85 consisting of dacitic lava flows and explosive breccia, is located at Fort Napoléon. The second phase,
86 dated at 2.40 ± 0.04 Ma made of basic andesitic lava and phreato-magmatic flows associated with
87 two-pyroxene andesite, is widespread across the island. The third phase, between 2.08 ± 0.03 Ma and
88 2.00 ± 0.03 Ma, was mainly expressed by the formation of the 'Le Chameau' dacitic dome ($2.00 \pm$
89 0.03 Ma) and is associated with dykes.

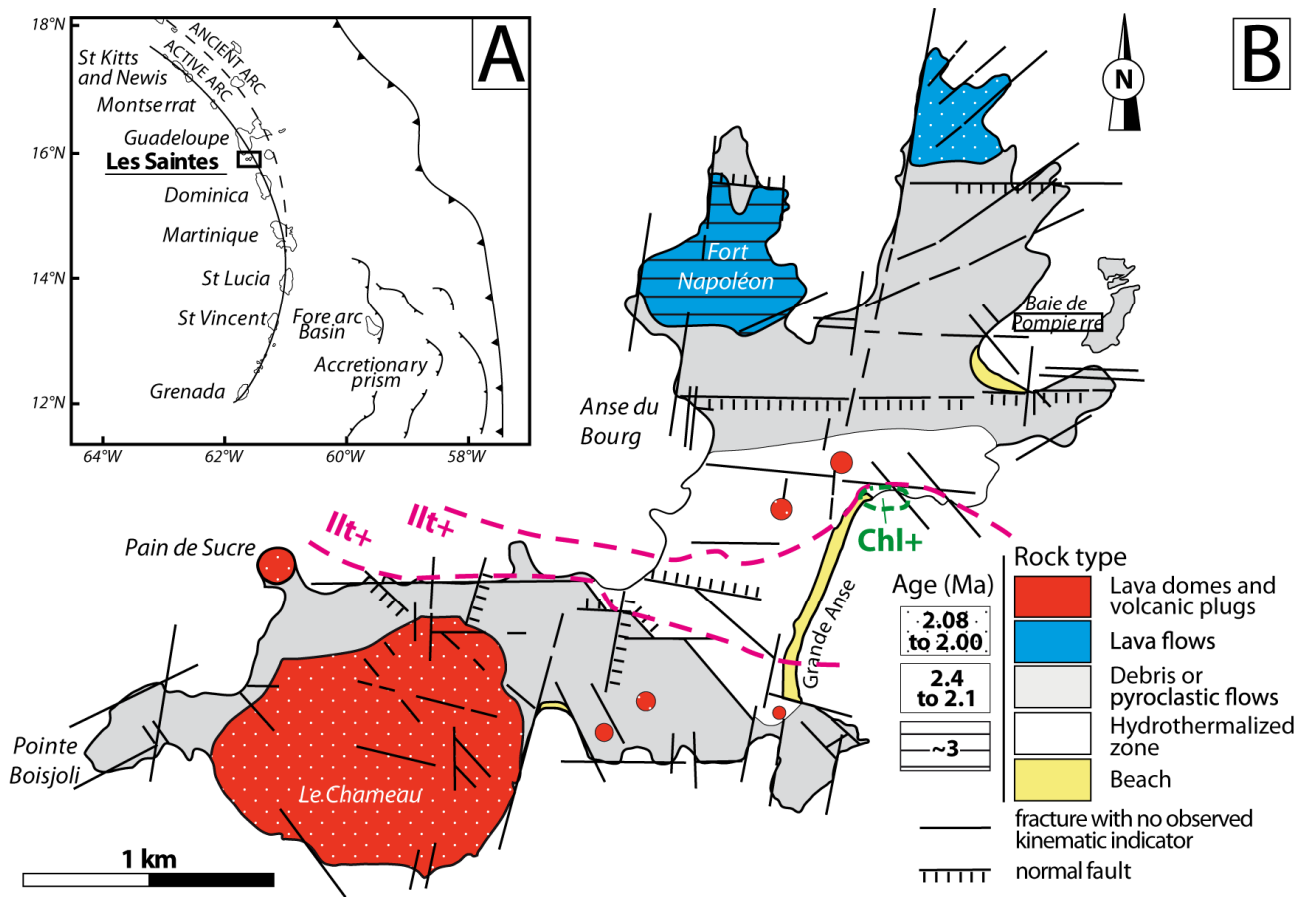
90 The occurrence of a hydrothermal zone has been identified and described long ago (Jacques et al.,
91 1984; Jacques and Maury, 1988a, b) and recently accurately documented (Verati et al., 2016).
92 According to Verati et al. (2016), the intersection of the two major normal fault systems N090-N110
93 and N130-N140 is responsible for the development of the hydrothermalized area, which is also the
94 case in the Bouillante geothermal field. This zone displays a succession of parageneses that are
95 characteristic of high-temperature hydrothermal alteration in epithermal settings and its retrogression
96 during cooling. Verati et al. (2016) observed a first high-temperature mineral assemblage composed
97 of (i) aggregates of chlorite and epidote developed as pseudomorphs from primary plagioclase and
98 clinopyroxene, or (ii) chlorite, serpentine and oxide aggregates formed at the expense of
99 orthopyroxene. The pseudomorphosed minerals are crosscut by millimetric veinlets filled by quartz
100 \pm chalcedony \pm pyrite \pm chlorite \pm smectite \pm goethite aggregates. Sometimes, the veinlets connect
101 vesicles filled with chalcedony and zeolites. According to Verati et al. (2016) a final advanced argillic

102 alteration stage generated kaolinite, illite, smectite, and, in the most altered samples, gypsum and
103 jasper are found.

104 In their study of clay mineral assemblages in the hydrothermal zone of Terre-de-Haut, Beauchamps
105 et al. (2019) showed a zonation with isograds of illite and chlorite appearance (Figure 1B). This clay
106 mineral distribution is commonly observed in geothermal contexts and is similar to that observed
107 vertically in Bouillante's boreholes.

108 From a petrophysical point of view, Navelot et al. (2018) and Beauchamps et al. (2019) show that
109 within the central hydrothermal zone, pathways for the fluids are encountered at all scales, from the
110 micrometre scale (μm -scale) through microcracks within phenocrysts, at grain joints and between
111 clay crystallites, to the metre- and kilometre-scale (m- and km-scale) thanks to fractures and faults.

112 According to Verati et al. (2016), the age of hydrothermalism is constrained within a time span
113 because the oldest volcanic rocks affected by the hydrothermal activity are dated at 2.40 ± 0.04 Ma
114 (Zami et al., 2014), and none of the most recent volcanic plugs dated at 1.94 ± 0.10 Ma by Jacques et
115 al. (1984) is hydrothermally altered, even when located in the hydrothermally altered zone (Figure
116 1B). The maximal timescale activity of the Les Saintes paleo-geothermal system is about 400 ky
117 according to Verati et al. (2016), whilst Zami et al. (2014) suggest that the hydrothermal activity
118 lasted around 80 ky between 2.08 ± 0.03 and 2.00 ± 0.03 Ma.



119

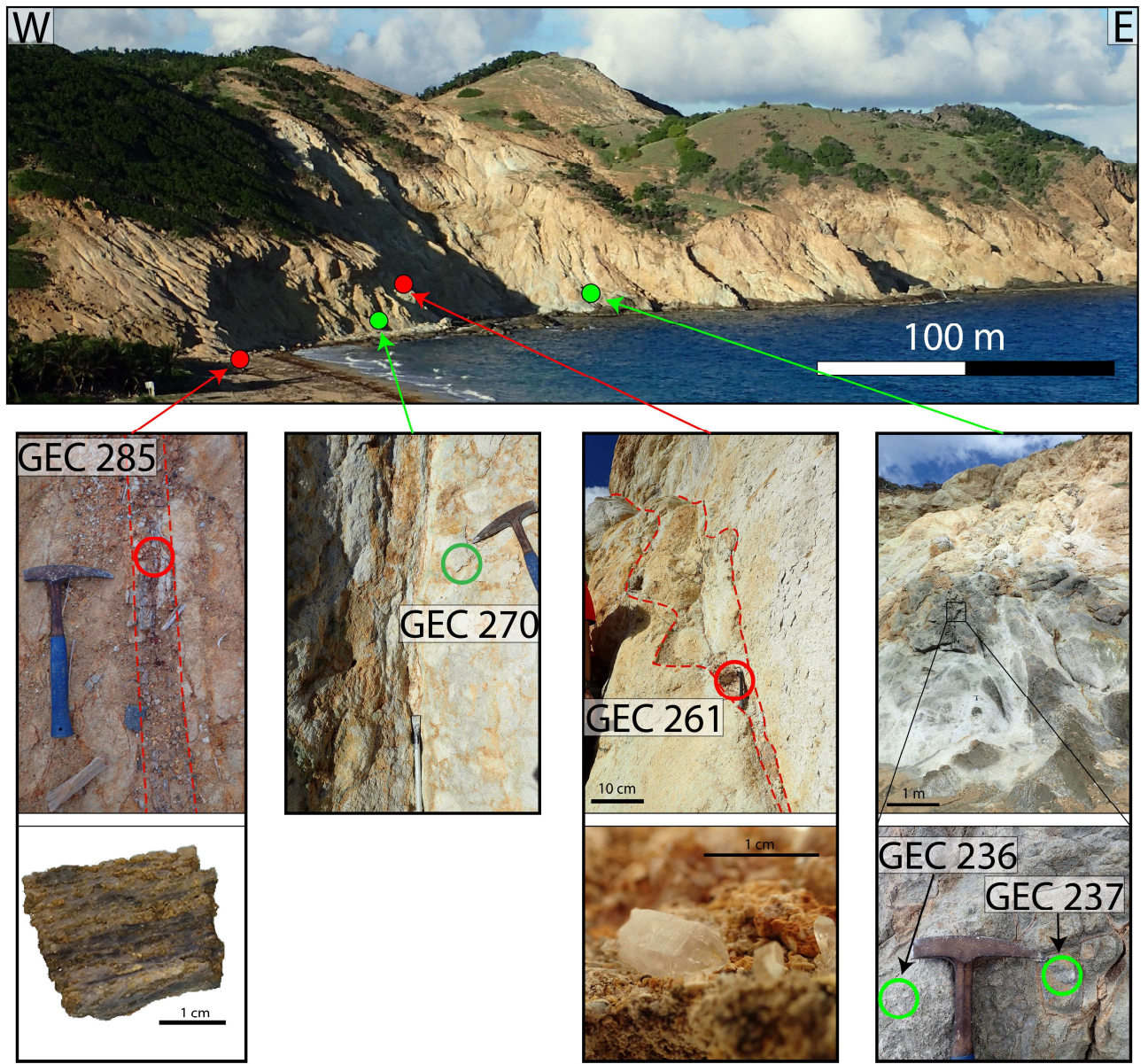
120 Figure 1 - A: Simplified geodynamic map of the Lesser Antilles Arc. B: Simplified geological map of Terre-de-Haut (Les
 121 Saintes archipelago) indicating structural data, volcanic rock types and their ages (modified after Verati et al. 2016; Zami
 122 et al. 2014; Jacques and Maury 1988a, b; Jacques et al. 1984). Symbols refer to age of the rock formation, whereas colours
 123 refer to rock type. Isograds of illite (Illt) in pink and chlorite (Chl) in green refers to Beauchamps et al. (2019).

124

125 3. Material and methods

126 3.1. Material

127 The samples analysed in this study come from the most hydrothermally altered zone (Jacques
 128 et al., 1984; Jacques and Maury, 1988a, b; Verati et al., 2016; Beauchamps et al., 2019), and more
 129 precisely from the northern part of Grande Anse (Figures 1 and 2). This zone, which corresponds to
 130 the ‘chlorite zone’ defined by Beauchamps et al. (2019) and its close vicinity, is hundreds of meters
 131 in size. This area presents a friable and yellowish general aspect where the initial andesite is no longer
 132 identifiable (Figure 2).



133

134 Figure 2 – Panoramic photograph of the outcrop of North Grande-Anse beach. White stars: sampling location. Focus on
 135 every sample on the outcrop and hand specimens is provided. Red dashed lines represent fractures limits.

136 GPS coordinates for the samples: GEC 285 - 15°51'59.29"N 61°34'37.40"O; GEC 270 - 15°52'02.27"N 61°34'35.27"O;
 137 GEC 261 - 15°52'03.45"N 61°34'33.34"O; GEC 236 and 237 - 15°52'04.03"N 61°34'30.34"O

138

139 *Chlorite-bearing samples*

140 Three chlorite-bearing samples are analysed in this study, noted GEC 236, GEC 237 and GEC
 141 270. GEC 236 and GEC 237 samples come from a dark zone of decametric size, harder than the outer
 142 yellowish country rock. This dark zone shows a network of centimetre-size fractures (Figure 2). The
 143 two samples are located twenty centimetres from one another.

144 Sample GEC 270 is located ~150 metres southwest of samples GEC 236 and 237 (Figure 2). It has
145 been collected twenty centimetres away from a fracture, in the host-rock. This rock presents a colour
146 from greyish to yellowish.

147

148 *Neoformed quartz*

149 Two samples of neoformed quartz, GEC 261 and GEC 285, have been sampled in north part
150 of Grande-Anse (Figure 2) 170 meters away from one another, for fluid inclusion analysis. In details,
151 GEC 261 has been sampled in the fracture oriented N70; 80SE (strike; dip) of Figure 2. This fracture
152 is five centimetres thick filled with brecciated rock and aggregates of euhedral quartz in some places.
153 The zone where quartz crystals occur is wider, with a width of ten centimetres and a length of fifteen
154 centimetres, which could be interpreted as a pull-apart extension (Figure 2). Numerous euhedral,
155 prismatic, bipyramidal, millimetre- size quartz are observed in this zone and were individually
156 sampled (Figure 2).

157 Sample GEC 285 has been taken from a banded quartz vein about 10 cm thick, oriented N70;70SE
158 (strike;dip). The banding pattern is regular and made of 1 to 3 mm thick bands of quartz relatively
159 parallel to one another.

160

161 3.2. Methods

162 *X-ray Diffraction*

163 X-ray Diffraction (XRD) analyses were performed at the Institut de Recherche Criminelle de
164 la Gendarmerie Nationale de Cergy-Pontoise (IRCGN, France), on the <2 µm fraction. The XRD was
165 carried out using a Panalytical X'Pert3 Powder (CuKα radiation, 45 kV, 40 mA), with the following
166 acquisition parameters: an angular domain between 2.5 and 30°2θ for < 2 µm fraction, a step
167 increment of 2θ = 0.01°, a counting time per step of 0.6 s. The sample preparation used was similar
168 to that proposed by Holtzapffel (1985). Each <2 µm fraction sample was spread on a glass slide to

169 stack clay minerals on their basal planes. Each sample was analysed in two states: (i) air-dried (natural
170 state); (ii) glycolated for one night to allow swelling of specific clay minerals.

171

172 *Microscopy*

173 Microscopic observations have been done on thin sections using both optical microscopy and
174 scanning electron microscopy (SEM, Zeiss Gemini 300, EHT = 15kV) belonging to the Plateforme
175 Microscopies & Analyses, Federation I-Mat of the CY Cergy-Paris University (France).

176

177 *Electron microprobe*

178 Chemical analyses of chlorite were carried out with a CAMECA SX 100 electron microprobe
179 (EMP) equipped with wavelength dispersive spectrometers (WDS). The equipment belongs to CNRS
180 Research Federation Chevreul in Lille. The analytical conditions were the following: 15 nA, 15 kV,
181 spot size of 1 μm , counting time of 20 s/element. The analysed elements were Si, Al, Fe, Mg, Mn, Ti,
182 Ca, Na and K. The system was calibrated with albite for Na, orthoclase for Al and K, wollastonite for
183 Ca and Si, MgO for Mg, MnTiO₃ for Ti and Mn, and Fe₂O₃ for Fe. Prior to analyse, thin sections
184 were coated with carbon.

185 Numerous punctual analyses were performed to obtain satisfying results: 103 in sample GEC 236, 54
186 in sample GEC 237, and 60 in sample GEC270. EMP analyses with $\text{K}_2\text{O}+\text{Na}_2\text{O}+\text{CaO} > 0.85 \text{ wt } \%$
187 were rejected to avoid chlorite contamination (e.g. by smectitic layer). Only analyses with an oxide
188 weight % summing between 84.00 and 89.00 were considered as belonging to the chlorite group. The
189 chlorite structural formulas were calculated on the basis of 14 O atoms (per half formula unit).
190 Quantitative mapping with a resolution of 1, 2 or 3 $\mu\text{m}/\text{pixel}$ was performed on 4 chlorite crystals,
191 with 8 element analysis (Si, Al, Fe, Mg, Mn, Ca, Na and K).

192

193 *Chlorite geothermometry*

194 Chlorite geothermometry was applied on the Terre-de-Haut chlorites in order to estimate the
195 temperature of their crystallisation. The used geothermometer was developed by Bourdelle et al.
196 (2013) specifically for low-T and low pressure contexts ($T < 350^{\circ}\text{C}$ and pressures below 4 kbar). It
197 is a semi-empirical thermometer based on a ratio of end-member activities and directly linking the
198 temperature to a K equilibrium constant for a chlorite + quartz equilibrium. This choice was driven
199 by the low P-T conditions prevailing in the studied area, and the Si-rich composition of the Terre-de-
200 Haut chlorites ($\text{Si} > 3$ apfu) preventing from the use of thermodynamic models as that developed by
201 Lanari et al. (2014). In addition, Bourdelle et al. (2013)'s thermometer does not require a prior
202 quantification of the Fe^{3+} content, assuming that all iron is divalent.

203 The formulation of the thermometer of Bourdelle et al. (2013) considers Mg end-members following
204 the chlorite + quartz equilibrium:

205



207

208 The resulting calibrated thermometric equation is:

209

$$210 T(^{\circ}\text{C}) = \frac{9400}{23.40 - \log K} - 273.15 \quad (2)$$

211

212 where K is the constant of the equilibrium (1). The thermometer was calibrated assuming H_2O and
213 SiO_2 activities as $a_{\text{H}_2\text{O}} = a_{\text{SiO}_2} = 1$. Considering the geological system studied here, the H_2O activity
214 could be considered as close to 1. Besides, $a_{\text{SiO}_2} = 1$ is justified in the case of quartz-bearing rocks.
215 In the same way, the pressure effect was neglected considering the hydrothermal context. The
216 accuracy of this geothermometer is estimated of $\pm 20^{\circ}\text{C}$.

217 To estimate the Fe^{3+} content in the studied chlorites, and the reducing or oxidizing nature of the
218 medium, a second geothermometer suitable to Si-rich chlorites from low-T contexts has been used
219 (Inoue et al. 2009). This thermometer has a similar basis that of Bourdelle et al. (2013), i.e. it is a
220 semi-empirical equation based on a ratio of end-member activities and a chlorite + quartz equilibrium.
221 However, the Inoue et al. (2009)'s thermometer needs the Fe^{3+} proportion to be quantified for each
222 chlorite analysis. That being difficult to obtain, the Fe^{3+} content was estimated by convergence of the
223 two thermometers. For this, several Fe^{3+} contents were tested, covering a $\text{Fe}^{3+}/\text{Fe}_{\text{total}}$ ratio = 0 to 40%
224 range. The results – and their sensibility to the Fe^{3+} content – are hereafter discussed. The
225 thermometric results are presented thanks to T-R²⁺-Si diagram (Bourdelle and Cathelineau, 2015).

226

227 *Fluid inclusion microthermometry*

228 Fluid inclusions (FIs) are relics of paleo-fluids trapped inside minerals during their growth.
229 The study of FIs allows characterising the paleo-fluid by determining its composition and the
230 pressure-temperature conditions during its entrapment. The validity of fluid inclusion analyses relies
231 on three basic assumptions: 1) the inclusions trapped a single, homogeneous phase; (2) the volume
232 of the inclusions has not changed since entrapment; (3) the composition of the inclusions remains
233 unchanged since it was trapped (Roedder, 1984).

234 FIs analysis is based on several methods: FIs petrography and typology, microthermometry,
235 spectroscopic methods. Observations are made on 100 μm thick double polished fluid inclusion
236 wafers. For euhedral quartz crystals, the sections have been realised parallel to the Z crystallographic
237 axis.

238 In this study, fluid inclusion analyses were performed at the Laboratory of Civil Engineering and geo-
239 Environment (LGCgE), University of Lille, using a FLUID INC. microthermometric stage (USGS
240 type). The calibration was done by measuring the melting temperature of CO_2 in synthetic aquo-
241 carbonic fluid inclusions and of ice in a pure water bath. At high temperature, calibration was done

242 using the homogenization temperature of pure critical H₂O (374.1°C). The maximum uncertainty
243 above room temperature was $\Delta=0.1^{\circ}\text{C}$ and $\Delta=1^{\circ}\text{C}$ at 400°C.

244 Here, the “Fluid Inclusion Assemblage” (FIA) approach (Goldstein and Reynolds, 1994) was used.
245 This method consists in gathering FIs all formed contemporaneously, by using only petrographic
246 criteria. According to Goldstein and Reynolds (1994), all the inclusions of a given FIA must have the
247 same composition, density and Th. A FIA is typically composed of 15 to 20 inclusions (Goldstein
248 and Reynolds, 1994). This statistical approach allows to eliminate data that diverge more than 10-
249 15°C from the average value.

250 Salinity based on the temperature of ice melting (T_{mi}) has been calculated using the equation of
251 Bodnar (1993). Homogenization temperature (T_{h}) represents the temperature at which one of the two
252 phases (liquid or vapour) disappears by dissolution in the other. The P-T conditions of entrapment
253 were estimated by calculating isochores that represent temperature evolution according to pressure,
254 assuming a constant volume. These isochores were calculated using the empirical equation of state
255 of Zhang and Frantz (1987).

256

257 *Cathodoluminescence*

258 Cathodoluminescence observations were done at the Earth Science Department, University of
259 Lille, using a cold cathode CITL 8200 MK IV mounted on a standard petrographic microscope.
260 Tension, vacuum and intensity are automated (between 8 and 27 kV for 200 to 800 mA). Photographs
261 are done with a Peltier cooled high resolution and low luminosity camera, Spot Flex produced by
262 Diagnostic Instrument. Exposure time was about 20 seconds.

263

264 *Raman*

265 Raman analyses were also performed at the Earth Sciences Department, University of Lille,
266 using a Horiba Jobin Yvon HR 800 UV Raman spectrometer. An Ar Lexel laser tuned at 532 nm was
267 used to reach excitation and the time for integration ranged from 180 to 600s. Raman was used to

268 characterise the volatile phase in fluid inclusions, i.e. the bubble density and its composition. For
269 single phase CO₂-fluid inclusion, density was estimated by measuring the spacing between the two
270 peaks of Fermi diad bands (Yamamoto et Kagi, 2006, 2008). The calibration of the device has been
271 done according to Dubessy et al. (1989) and Burke (2001) procedure to calculate the molar fraction
272 of the different gas species from the area of the spectrum peaks.

273

274 **4. Results**

275 4.1. Petrography

276 *Optical microscopy*

277 The initial mineralogical assemblage, prior to alteration, was constituted by microlithic
278 groundmass, with phenocrysts of plagioclase, clinopyroxene and orthopyroxene of millimetric size
279 with a euhedral shape. Titanomagnetite was also part of the primary mineral assemblage.

280

281 GEC 236 and GEC 237:

282 The rock matrix is fully recrystallized into micro-crystalline quartz (Figure 3A, B, C, D). Phenocrysts
283 of plagioclase are mostly preserved, some of them show more or less intense static replacement by
284 calcite distributed randomly within the mineral.

285 Chlorite occurs as partial or complete primary pyroxene pseudomorph, their euhedral shape being
286 preserved (e.g. Figures 3A, B). Some pseudomorph are entirely composed of chlorite (Figure 3B),
287 some are composed by chlorite and patches of calcite (Figure 3A). Other chlorite minerals are present
288 in the matrix with a much smaller size (few micrometers), and on border of calcite veins (Figure 3D).

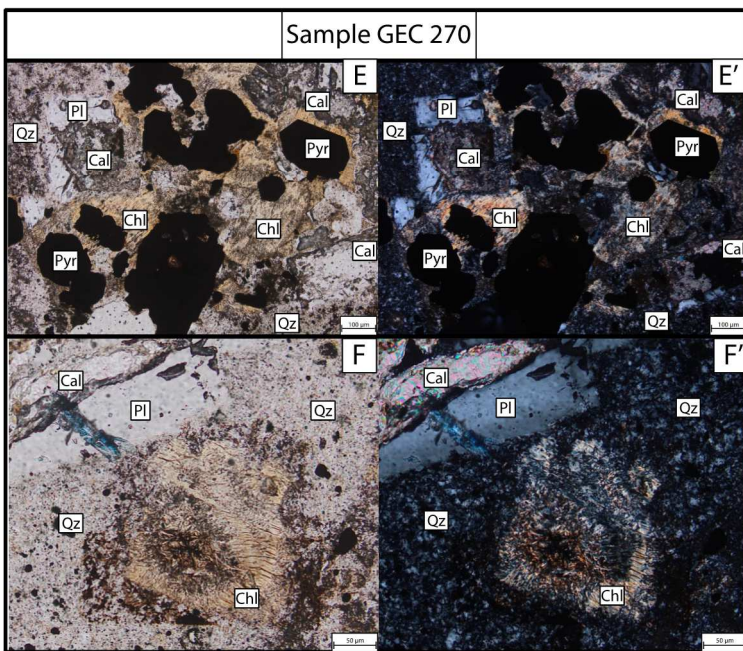
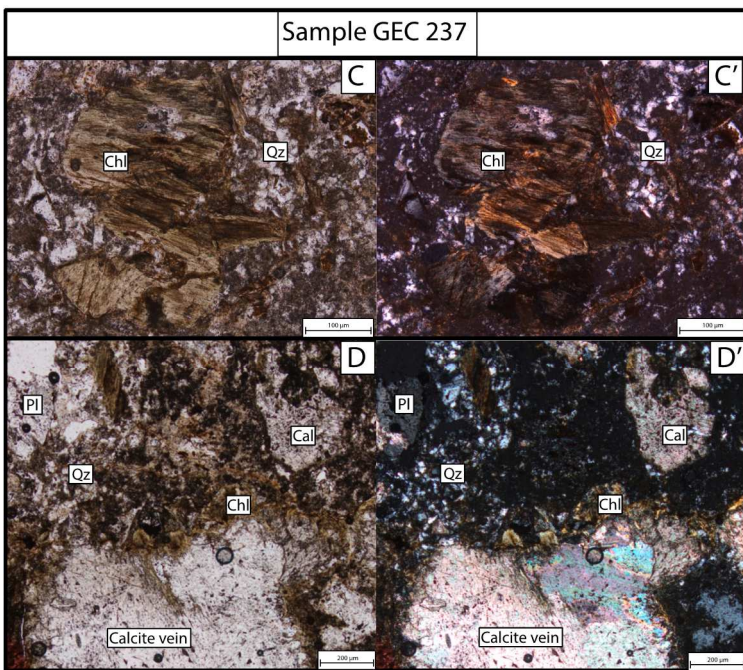
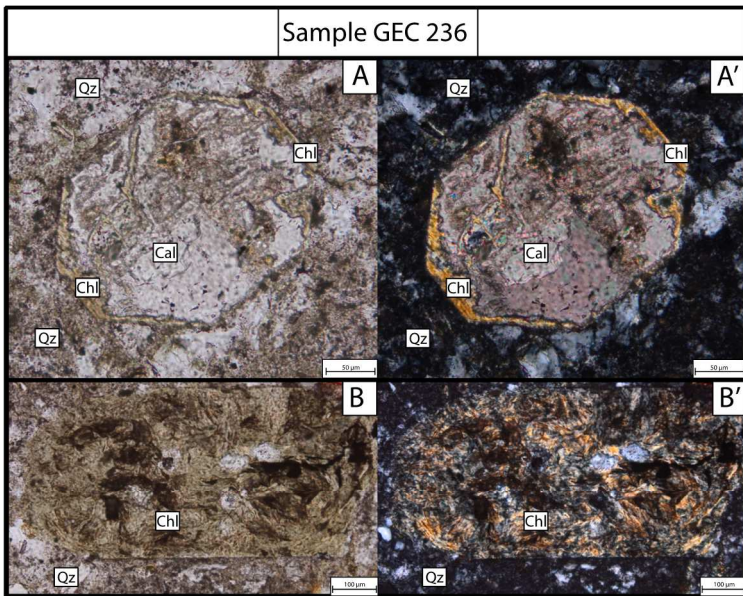
289 Rare epidote crystals are observed in the sample, with no geometric relationship with chlorite.

290 Microveins, up to 1 mm thick, constituted of calcite, pyrite, quartz, are present in sample GEC 237.

291

292 GEC 270:

293 Most of the plagioclase phenocrysts present a well-developed fracture network, sometimes showing
294 calcite pseudomorph. The matrix is totally made of micro-crystallized quartz like in GEC 236 and
295 GEC 237. Chlorite crystals, with sizes from 50 μm to 500 μm , show a light pleochroism. Although
296 the primary minerals are no longer present, the rectangular shape of some chlorite assemblages
297 suggest they are pseudomorphs after ancient primary pyroxenes (Figure 3F). Pyrite crystals from 50
298 μm to 200 μm , sometimes euhedral, are also present disseminated in the sample (Figure 3E).

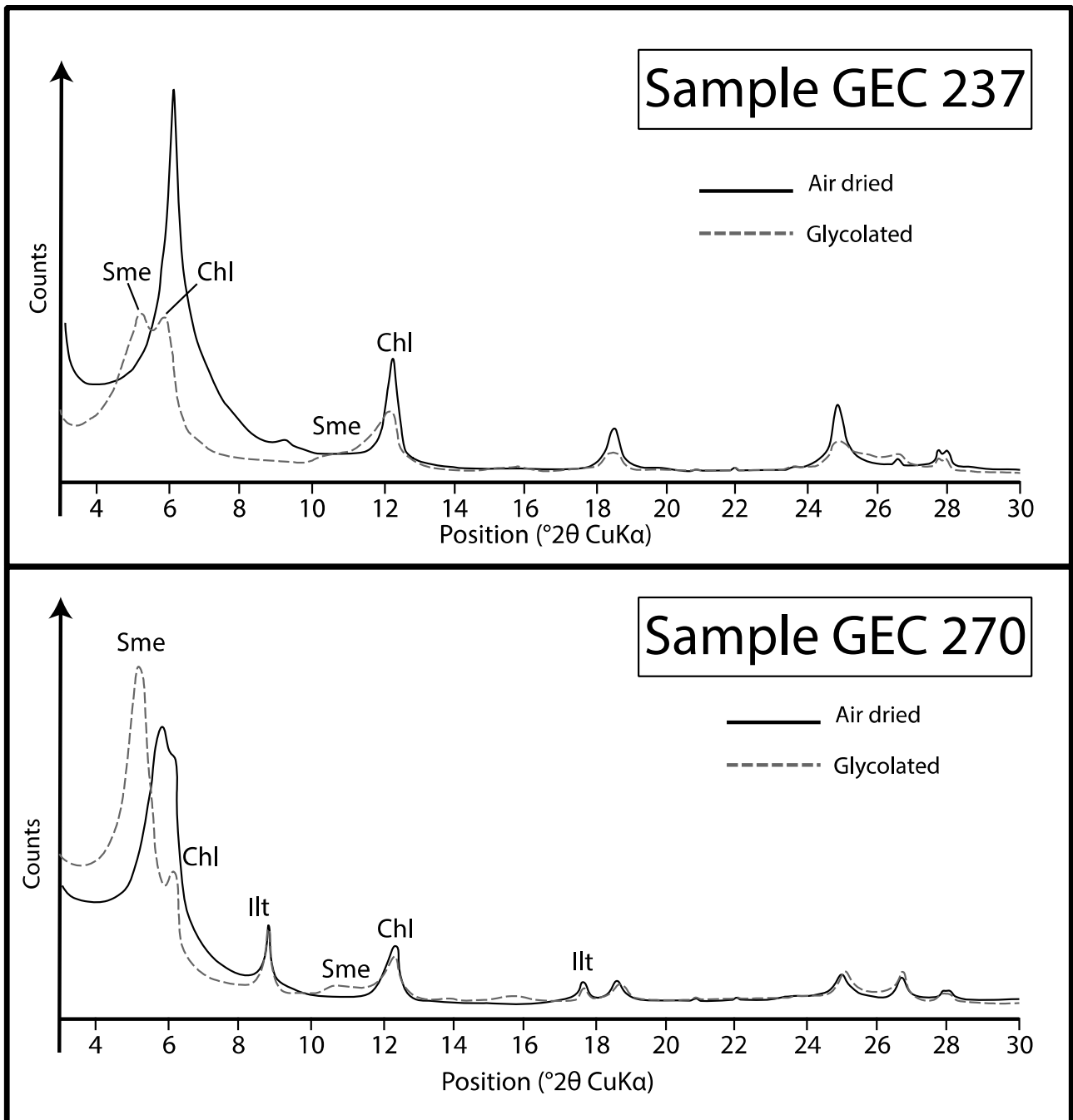


300 Figure 3 - Optical microscopy photograph with plane polarized light (X) and crossed polarized light (X') of samples GEC
301 236 (A, B), GEC 237 (C, D), and GEC 270 (E, F). Mineral abbreviations according to Whitney and Evans (2010).

302

303 *XRD*

304 X-Ray Diffraction analyses have been performed on the < 2µm fraction from samples GEC
305 236, GEC 237 and GEC 270. Sample GEC 270 shows an assemblage of smectite (Sme) + chlorite
306 (Chl) ± illite (Ill) as can be seen in Figure 4. For sample GEC 236 and GEC 237, the assemblage is
307 composed of smectite (Sme) + chlorite (Chl) as in Figure 4. However, regarding sample GEC 237, a
308 slight shift towards lower angles of the chlorite peak at the Ethylene-Glycol state (14.9Å) and the
309 non-symmetrical shape, reveals the presence of mixed-layers minerals with an expandable phase,
310 such as chlorite/smectite (C/S) mixed-layer mineral (Figure 4).



311

312 Figure 4 - X-ray diffractogram of the clay mineral assemblages of sample GEC 237 (G) and GEC 270 (H). (d(001) and
313 d(002) are indexed. Mineral abbreviations according to Whitney and Evans (2010).

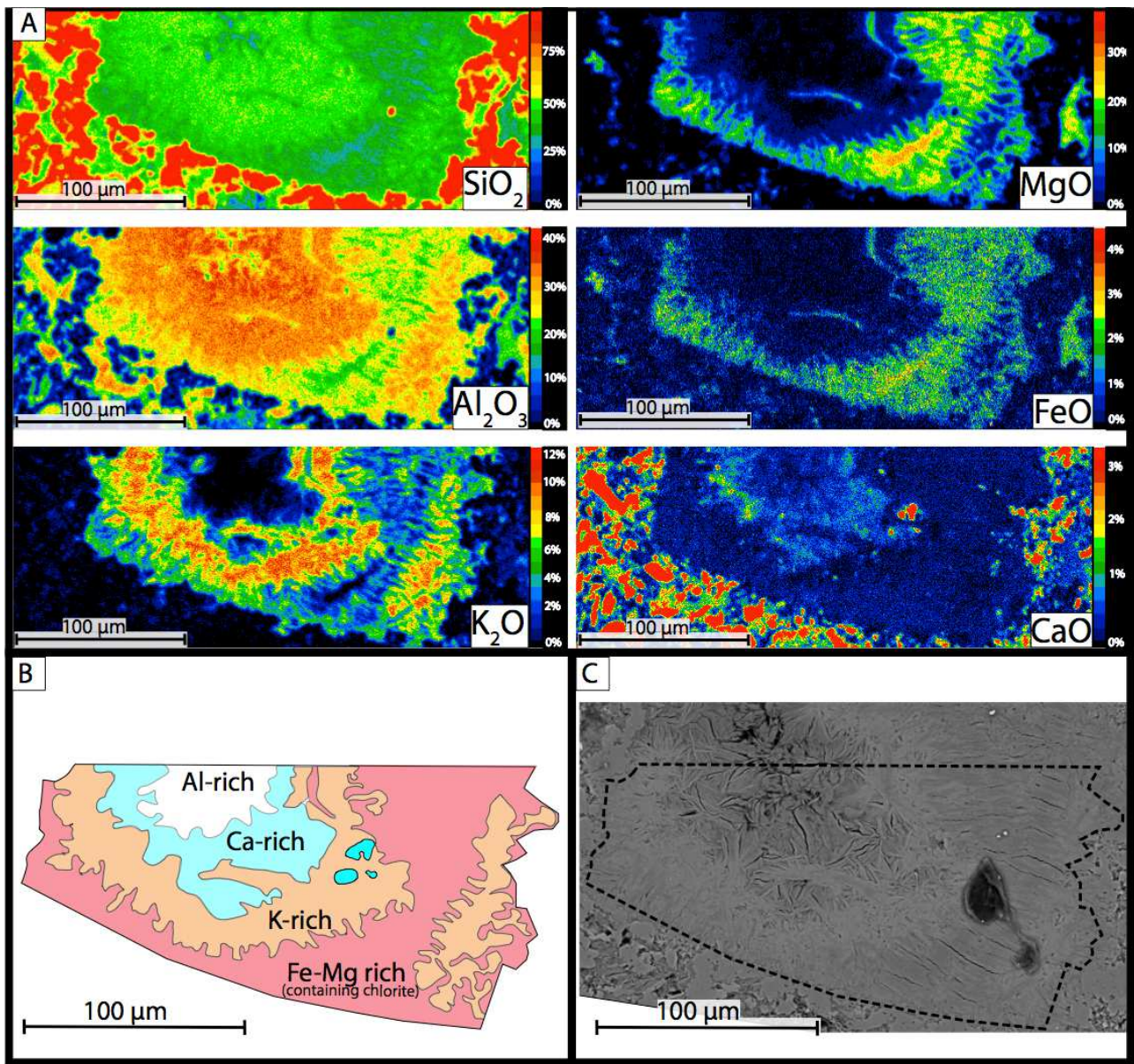
314

315 4.2. Chlorite study

316 *Chemical mapping and intra-mineral microstructure characterisation*

317 Chemical mapping has been performed in seven areas (3 in GEC 236; 1 in GEC 237; 3 in
318 GEC 270). The maps represent the oxide weight percentage of SiO₂, Al₂O₃, K₂O, MgO and FeO, by
319 a color scale.

320 Chemical mapping of chlorite pseudomorphs allows to observe chemical zonations in a totally
321 transformed primary mineral. Figure 5A displays results of such a mapping of the mineral presented
322 in Figure 3F (sample GEC 270). As observed in Figure 5A, composition of the altered primary
323 mineral is not homogeneous. First of all, the rectangular shape of the primary mineral is well visible
324 and the circular chemical zonation clearly highlighted. The core of the mineral presents only Si and
325 Al, the first inner ring is rich in Si, Ca and Al. The second inner ring shows an enrichment in K; a
326 third ring shows a depletion in K, Al and Si, associated to an enrichment in Fe, Mg and Mn (not
327 represented here). The outer ring is similar to the second ring with the well visible enrichment in K.
328 These chemical variations are synthesized in Figure 5B. Therefore, only Si and Al in the core of the
329 mineral suggest the presence of kaolinite. Ca in the first inner ring might show a residual composition
330 of a Ca-rich pyroxene, which is consistent with the occurrence of augite in this type of rocks (Jacques
331 et Maury, 1988b), or a smectitic composition. K enrichment in the second and outer rings is due to
332 the presence of illitic phase, and the enrichment in Fe and Mg in the third ring leads to chlorite phase.
333 This zone has been investigated through scanning electronic microscopic observations showing this
334 pseudomorph mineral presents multiple contrasts, which are well related with the chemical sequence
335 previously described (Figure 5C).



336

337 Figure 5 – A: Chemical mapping done with Electronic Microprobe of a transformed primary volcanic mineral in sample
 338 GEC270. B: sketch synthesizing the chemical variation. Chlorite composition is found in the Fe-Mg rich zone. C:
 339 Scanning Electron Microscopy (SEM) image. (EHT: 15.00 kV; WD:9.4mm). Dashed line represents the border of the
 340 sketch in B.

341

342 *Chemical composition and chlorite thermometry*

343 Some representative analyses of chlorite are presented in Table 1, among the 75 that were
 344 considered of good quality (50 for GEC 236, 17 for GEC 237, 8 for GEC 270; available in
 345 supplementary material).

346

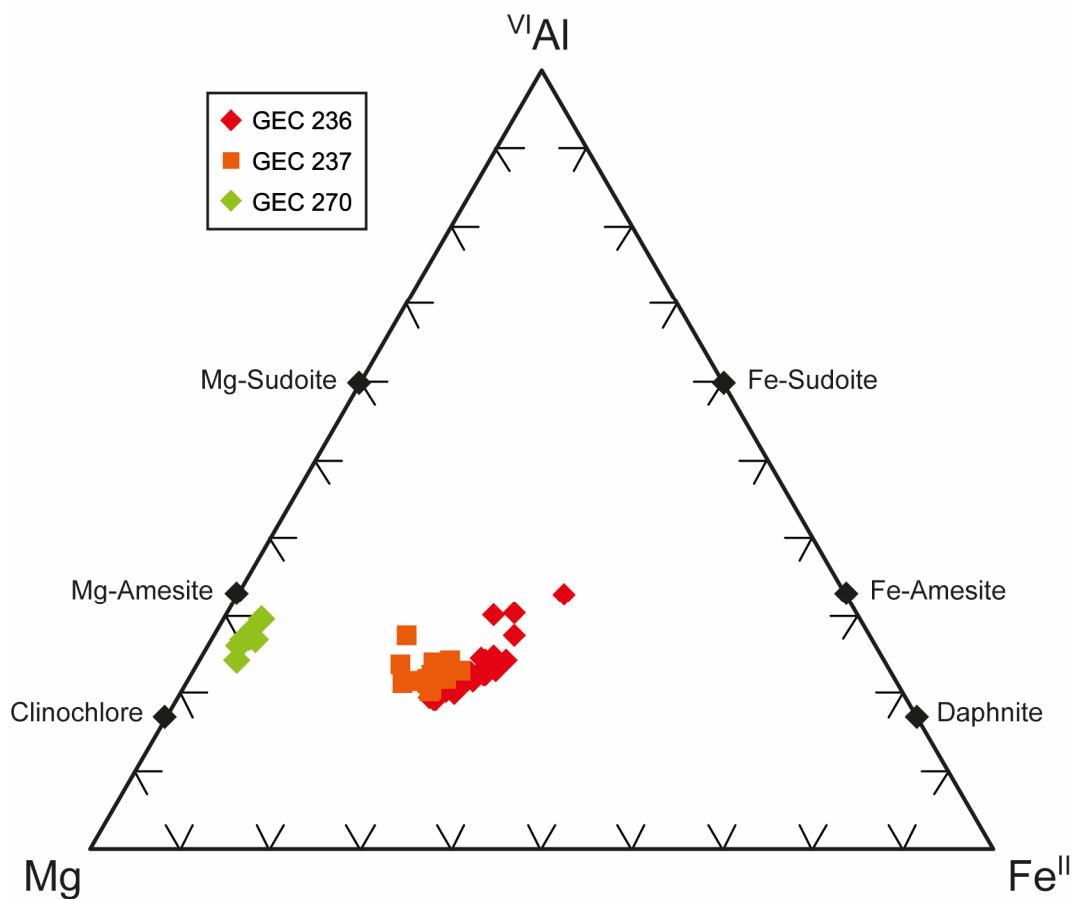
Sample	GEC 236		GEC 237		GEC 270	
	z1	z2	z5	z6	z7	z9
Oxide weight %						
SiO ₂	31.89	31.52	32.96	31.99	35.63	35.13
TiO ₂	0.03	0.00	0.01	0.03	0.11	0.14
Al ₂ O ₃	16.60	15.75	16.77	15.98	20.02	19.86
FeO	20.62	19.10	16.43	17.99	2.50	2.97
MnO	0.66	0.53	0.64	0.58	0.47	0.54
MgO	16.82	18.18	20.54	18.04	27.02	29.31
CaO	0.66	0.48	0.44	0.65	0.31	0.23
Na ₂ O	0.10	0.02	0.07	0.03	0.04	0.07
K ₂ O	0.02	0.07	0.06	0.04	0.32	0.13
Total	87.39	85.66	87.92	85.34	86.41	88.37
CaO+Na ₂ O+K ₂ O	0.78	0.57	0.57	0.72	0.79	0.43
apfu (O ₁₄)						
Si	3.26	3.27	3.27	3.31	3.32	3.22
Ti	0.00	0.00	0.00	0.00	0.01	0.01
Al	2.00	1.93	1.96	1.95	2.20	2.15
Fe ^{II}	1.76	1.66	1.36	1.56	0.19	0.23
Mn	0.06	0.05	0.05	0.05	0.04	0.04
Mg	2.57	2.81	3.04	2.78	3.76	4.01
Ca	0.07	0.05	0.05	0.07	0.03	0.02
Na	0.02	0.00	0.01	0.01	0.01	0.01
K	0.00	0.01	0.01	0.01	0.04	0.02

347

348 Table 1 – Representative chemical analyses obtained by electron microprobe on chlorite crystals (apfu = Atoms Per
349 Formula Unit).

350

351 Microprobe analyses show that all these chlorites are Si-rich ($3.1 \leq \text{Si} \leq 3.4$ apfu; Table 1), with an
352 Al content of around 2 apfu. Only Fe/Mg ratio shows variations (Figure 6): in GEC 236 and GEC237
353 samples, chlorites are ferromagnesian (XFe is around 0.39 ± 0.1 for GEC 236, and around 0.34 ± 0.05
354 for GEC 237), whereas chlorites in GEC 270 are magnesian, characterised by a XFe of 0.09 ± 0.2 .
355 These two different chlorite compositions are clearly observed in a Mg-Fe^{II-IV}Al diagram (Figure 6).



356

357 Figure 6 - Chlorite octahedral content plotted in a ternary diagram (Mg, ^{VI}Al, Fe^{II}). Red: GEC236; Orange: GEC 237;

358 Green: GEC 270

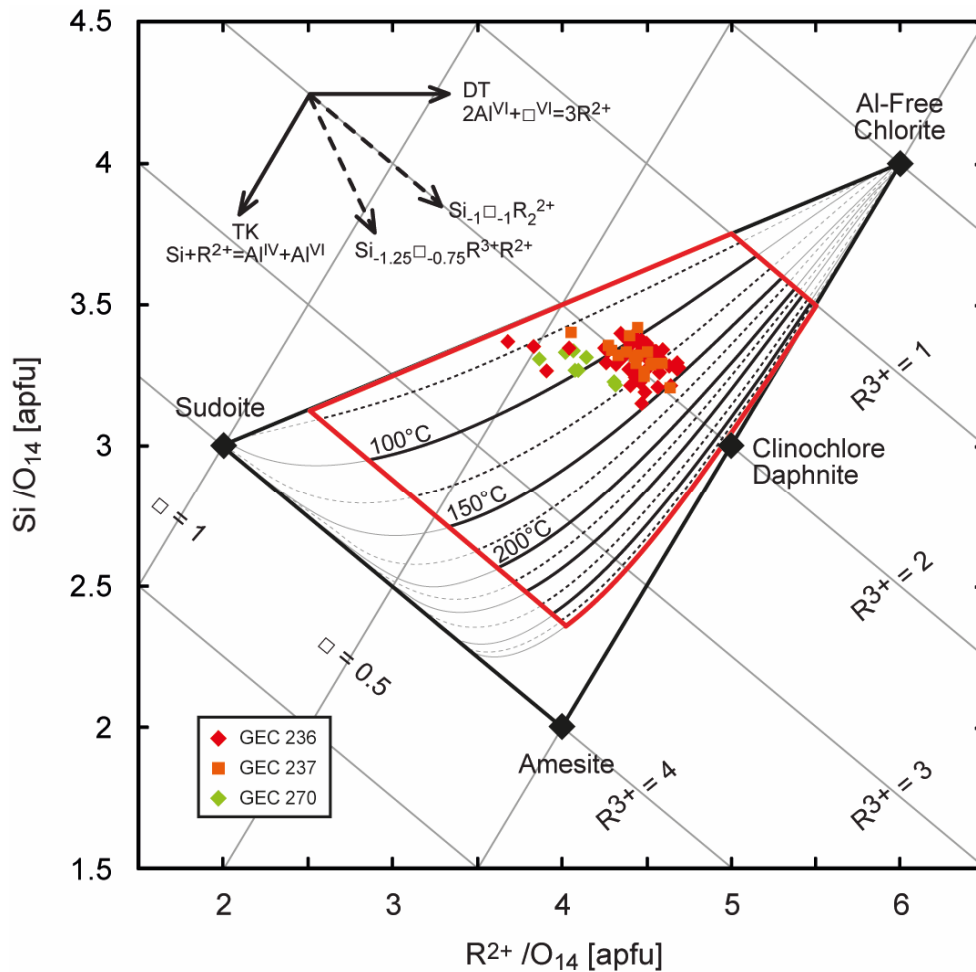
359

360 GEC 237 chlorite compositions draw a trend towards Fe-Sudoite while GEC 236, sampled 20 cm
 361 away, shows a more homogeneous group of compositions. But both groups of composition are grossly
 362 overlapped. Conversely, GEC 270 sample chlorites have a very low Fe content.

363

364 Temperature calculations using the geothermometer developed by Bourdelle et al. (2013), on 18
 365 chlorites, show a temperature range from 72°C to 158°C with an average temperature of 120°C
 366 (Figure 7). The majority of the T estimates are grouped around 120°C, with R³⁺ = 2, while only few
 367 measures (and especially those for GEC 270) are trending towards less R²⁺ - lower T°C. This could
 368 be correlated to the amount of Ca and K in these chlorites, suspecting a possible mixing with smectite
 369 or illite, beyond the chemical criteria applied to select the chlorite analysis.

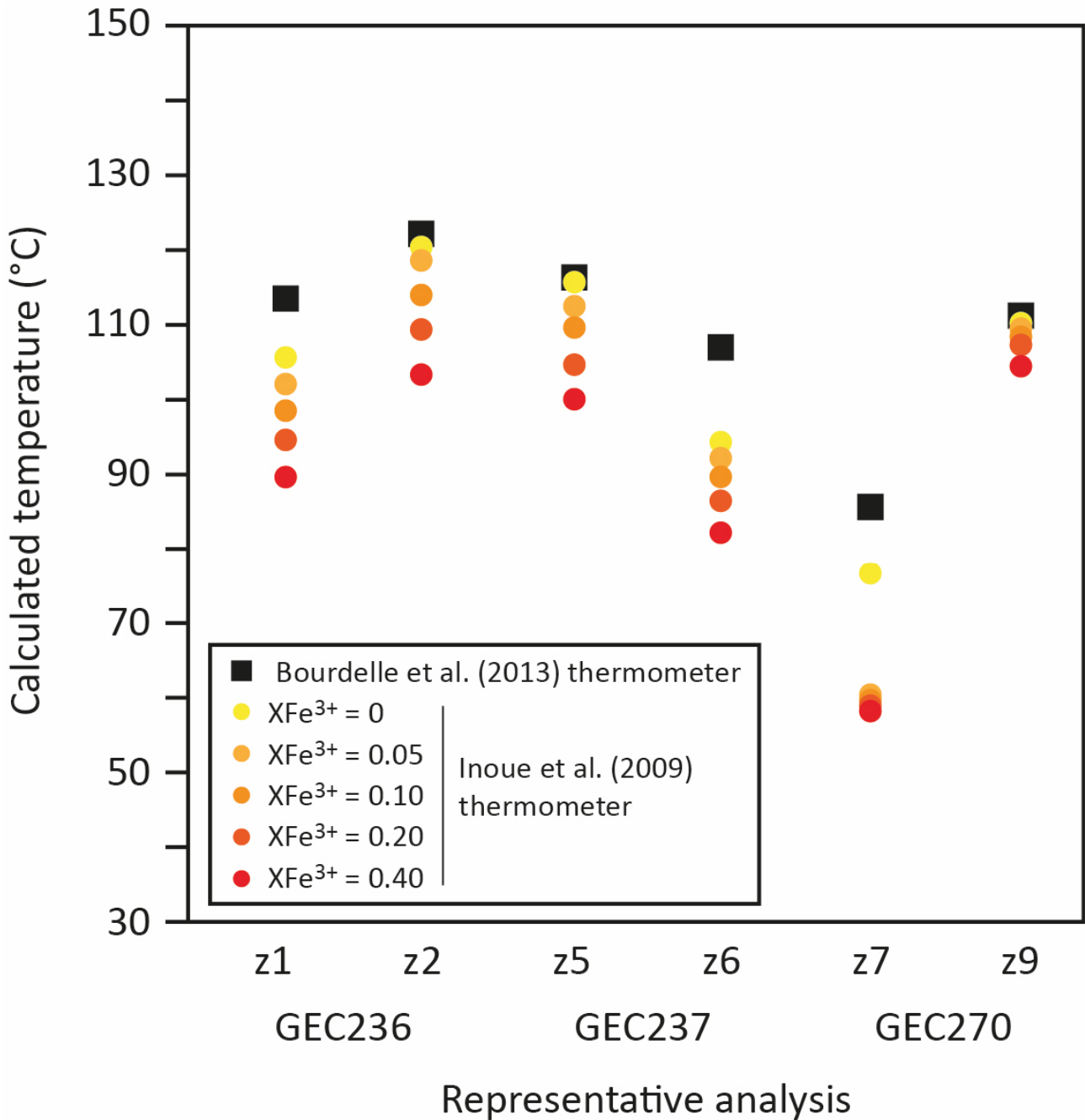
370 Chlorites display no zonation in terms of temperature. Temperatures obtained in the core or in the
 371 border of the minerals are similar.



372
 373 Figure 7 - Si-R²⁺ diagram developed by Bourdelle et al. (2015) showing the location of the samples analysed in this study
 374 (GEC 236 in red, GEC 237 in orange, GEC 270 in green).

375
 376 Temperature calculations have also been performed using the thermometer developed by Inoue et al.
 377 (2009). Temperatures obtained for the representative analyses are shown in Figure 8. The major
 378 difference with the thermometer developed by Bourdelle et al. (2013), is that the one of Inoue et al.
 379 (2009) requires a prior estimation of the Fe³⁺ content of the chlorite. As this element cannot be
 380 quantified by WDS, the Fe³⁺ content was estimated by the convergence of the two thermometers,
 381 with the temperatures calculated with the Bourdelle's thermometer as a reference. For this, various
 382 contents of Fe³⁺ have been tested (Figure 8). The difference between temperatures obtained by the
 383 two geothermometers is in average less than 30°C. Considering the error range of ±20°C of each

384 geothermometer, the difference of 30°C is less than the two errors accumulated (Figure 8) and tends
 385 to show the robustness of the T estimates. Moreover, the minimum differences between the two
 386 geothermometers are observed when $X\text{Fe}^{3+}$ (i.e. $\text{Fe}^{3+}/\text{Fe}_{\text{total}}$) value is equal to 0.00. This allows
 387 supposing that $X\text{Fe}^{3+}$ in these chlorites is very low, and that the medium is not oxidizing.



388
 389 Figure 8 - Temperature estimations for representative chlorite analyses using both Bourdelle et al. (2013)'s and Inoue et
 390 al. (2009)'s geothermometers. For Inoue et al. (2009)'s geothermometers, different $X\text{Fe}^{3+}$ values have been tested.

391

392 4.3. Microthermometry on fluid inclusions in quartz crystals

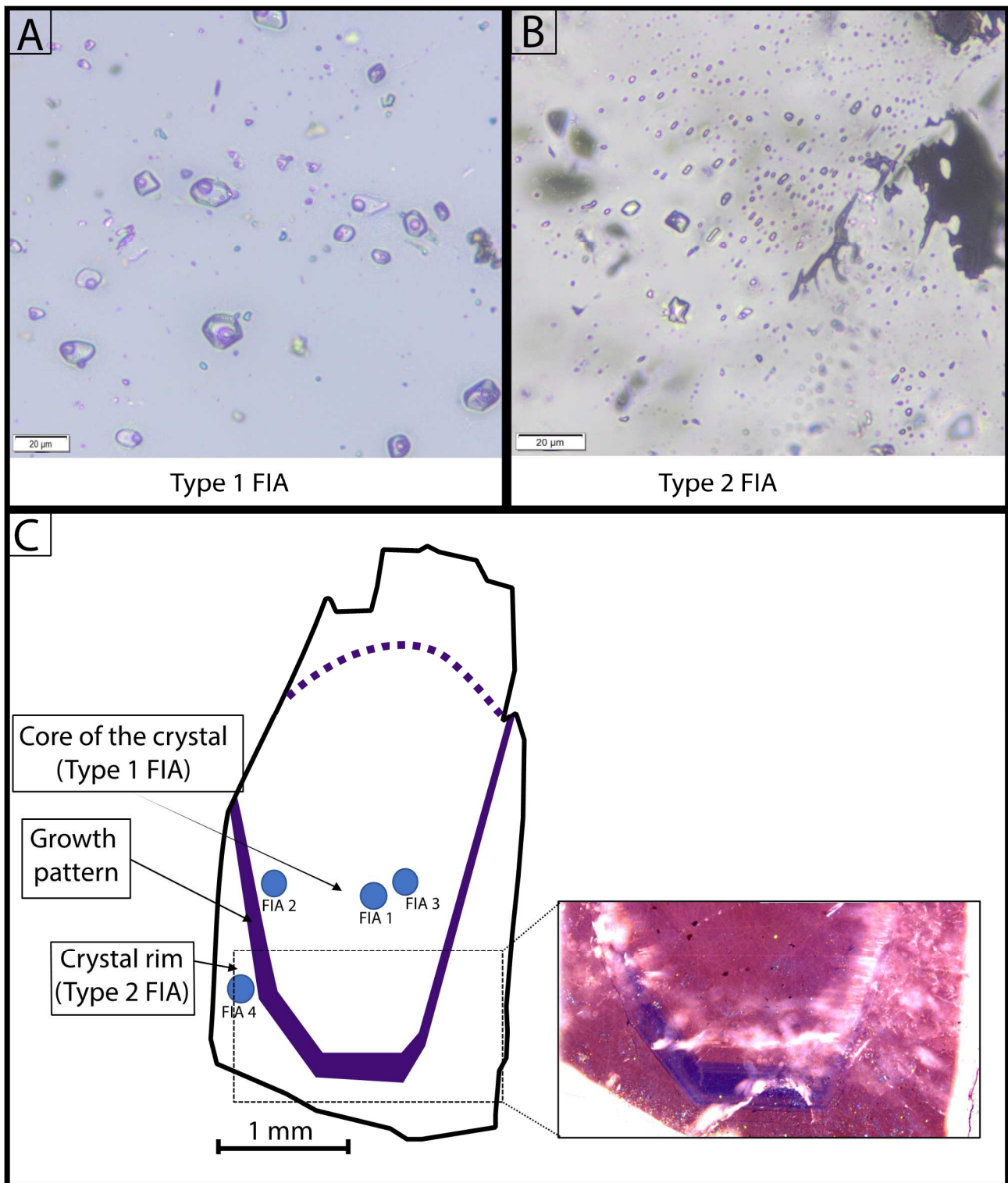
393 *Sample GEC 261*

394 Using the approach developed by Goldstein and Reynolds (1994) and based on the vapour
395 filling ratio (Flv), two types of FIAs can be distinguished in GEC 261 sample (Figure 9 A, B):

396 -Type #1 contains only two phases (liquid+vapour; LV) with consistent Flv of about 20% (Figure
397 9A).

398 -Type #2 is composed of all-liquid (L) fluid inclusions associated with rare two-phase LV inclusions
399 with variable Flv (Figure 9B).

400 Inclusion sizes vary from about 10 μm to up to 40 μm , and their shape is generally oval, and
401 sometimes hexagonal or complex. A crystal fragment of sample GEC 261 is a key sample to
402 understand FIAs distribution and relative chronology. Figure 9C is a representation of the 5 mm-long
403 longitudinal section. This crystal fragment has been studied by microscopy and cathodoluminescence,
404 revealing a clear zoning. The core of the crystal hosts FIAs of type #1 inclusions (respectively FIAs
405 1, 2 and 3), whereas the outer zone of the crystal contains FIA composed of type #2 inclusions (FIA
406 4; Figure 9C). Inclusions are undoubtedly of primary origin, indicating that they formed during
407 crystallization of quartz.



408

409 Figure 9 - A: Photograph of type #1 FIA. B: Photograph of type #2 FIA. C: Crystal fragment n°2 with
 410 cathodoluminescence photograph showing the intra-crystal zonation.

411

412 In type #1 FIAs, ice melting temperatures (T_{mi}) are comprised between -0.2°C and -1.1°C for the
 413 whole set of inclusions, corresponding to salinities of 0.4 to 1.9 wt % eq. NaCl respectively. The

414 eutectic melting has not been observed because of the low salinity of the fluid. The homogenization
 415 temperatures (Th) are comprised between 230 and 280 °C. The mean Th per FIA are within 240°C
 416 and 271°C (Table 2). The low standard deviation (less than 14°C per FIA) means that inclusions were
 417 not affected by post-trapping processes.

418 Regarding type #2 FIAs, Goldstein and Reynolds (1994) demonstrated that FIAs containing both LV
 419 and L inclusions, where all-liquid inclusions are not paired with two-phase inclusions but in the same
 420 size range, testify of a formation temperature lower than 50°C. Tmi was measured only in the two-
 421 phase inclusions as the liquid-vapour equilibrium makes Tmi directly open to interpretation in terms
 422 of salinity. Tmi values are comprised between 0 and -1.0°C, corresponding to a salinity of less than
 423 1.7 wt % eq. NaCl. Th was not measured as they do not represent temperature-pressure trapping
 424 conditions (see discussion below).

425

FIA type	Crystal fragment n°	FIA n°	Number of FI	Tmi (°C)			Th (°C)		
				Mean	Standard deviation	Calculated salinity (wt% eq. NaCl)*	Mean	Standard deviation	
Crystal Core	#1	1	16	-0.7	0.2	1.2	268	6	
		2	15	-0.4	0.1	0.8	256	14	
		3	6	-0.7	0	1.3	271	13	
		13	1	11	-0.4	0.1	0.6	240	10
		10	1	9	-0.5	0.1	0.9	267	6
Crystal rim	#2	2	4	-0.8	0.1	1.4			
		3	1	13	-0.8	0.1	1.4		
		11	1	3	0.7	0.1	1.2		
		13	2	6	-0.4	-	0.7		
		14	1	4	0	0	0		

426

427 Table 2 – Synthetic table of the different measures done on the different crystals of the sample GEC 261.
 428 (Tmi=Temperature of ice melting; Th= Homogenization temperature). * Bodnar (1993).

429

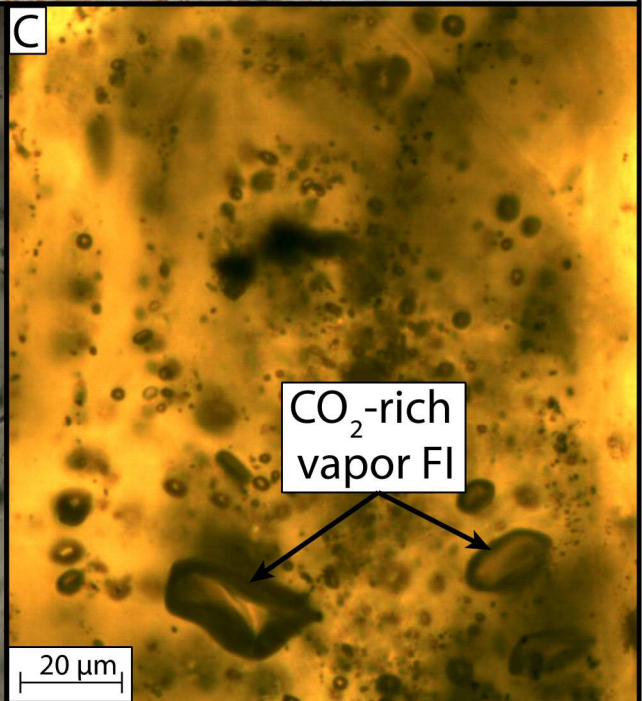
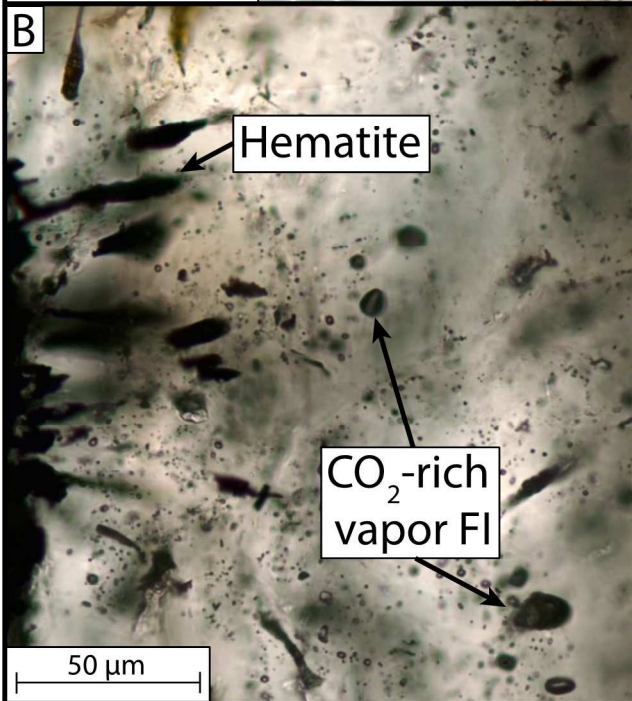
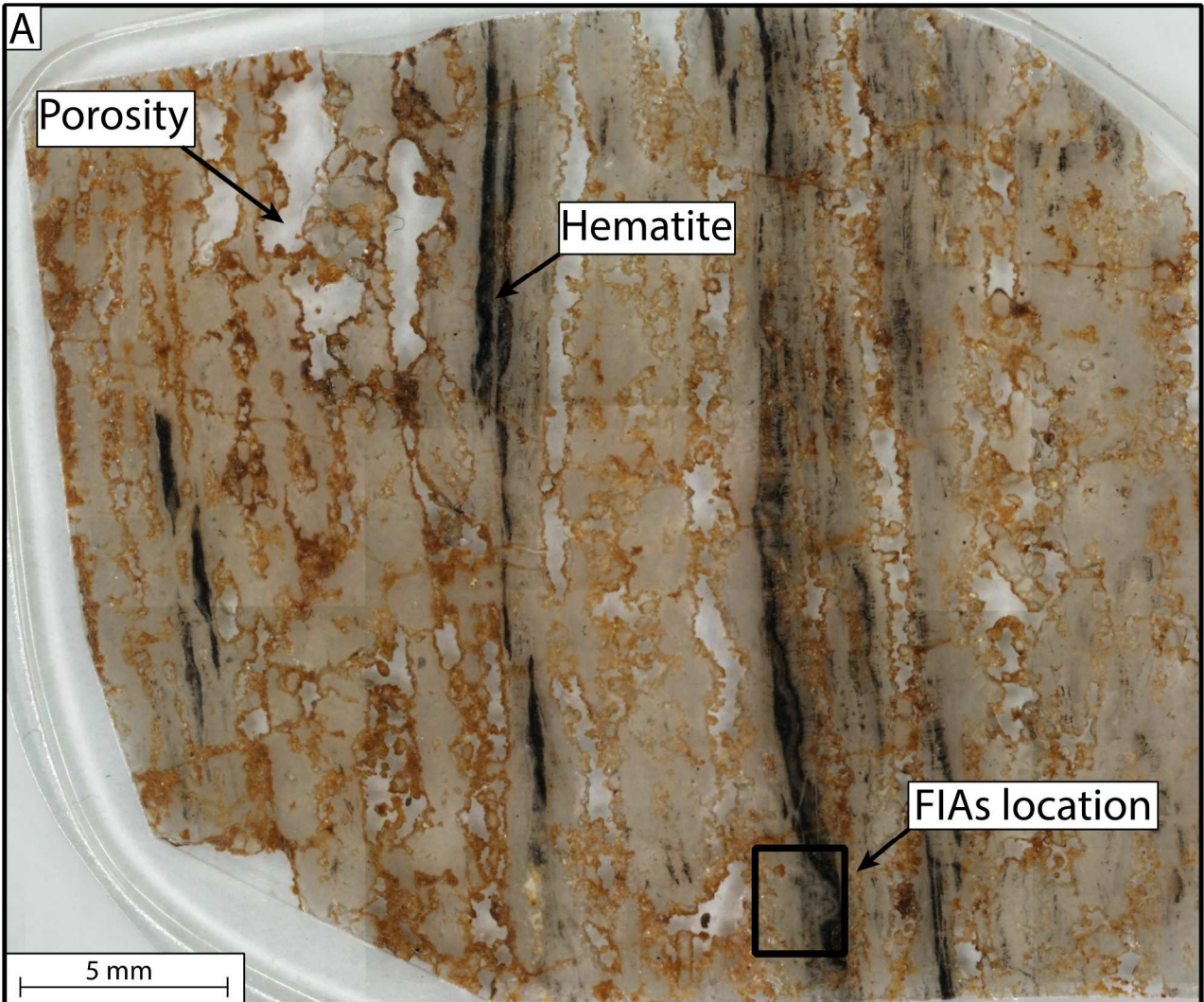
430 Microthermometric data indicate that the fluid trapped in both inclusion types is almost pure water,
 431 salinity being less than 2 wt % eq. NaCl. Presence of gases, CO₂ among others, cannot be excluded.
 432 At first, the small size of vapour bubbles and their mobility at room temperature prevent any analysis

433 using Raman microspectrometry. Secondly, a cycling procedure was applied to try to detect the
434 presence of gas hydrates. Indeed, after the final ice melting temperature, a rapid cooling of inclusions
435 with a 2°C step was applied in order to observe the potential deformation or move of the vapour
436 bubble. Neither shape change nor move of the bubble were observed, which lead to neglect the
437 presence of any volatile component in the bubble. Phase relationships in the system H₂O-CO₂
438 (Diamond, 2003) however indicate that a maximum CO₂ concentration of 1 mol% could be allowable.
439 The distribution of the two types of fluid inclusions allows to establish a relative chronology and to
440 constrain the evolution of fluid properties. Hence, the fluid trapped in the crystal core has Th around
441 240-270 °C, which represents nearly trapping conditions as isochores in the H₂O-NaCl system are
442 nearly sub-vertical lines. The FIAs located in the rim of the crystal have recorded a later event, much
443 cooler, with temperatures probably below 50°C. The general trend of fluid evolution in quartz is
444 therefore the recording during quartz precipitation of a cooling process from a first episode at 240-
445 270°C to a second episode at less than 50°C, with a relatively low salinity probably referring to a
446 mixing between meteoric and sea waters.

447

448 *Sample GEC 285*

449 In this sample, quartz bands sometimes show gulf-like pattern. A large amount of residual
450 porous space can be observed, partially occupied by euhedral quartz (Figure 10A). Laminae of
451 hematite, as identified with Raman, are incorporated within the quartz bands; They present an
452 elongated heel shape, perpendicular and associated to the quartz vein.



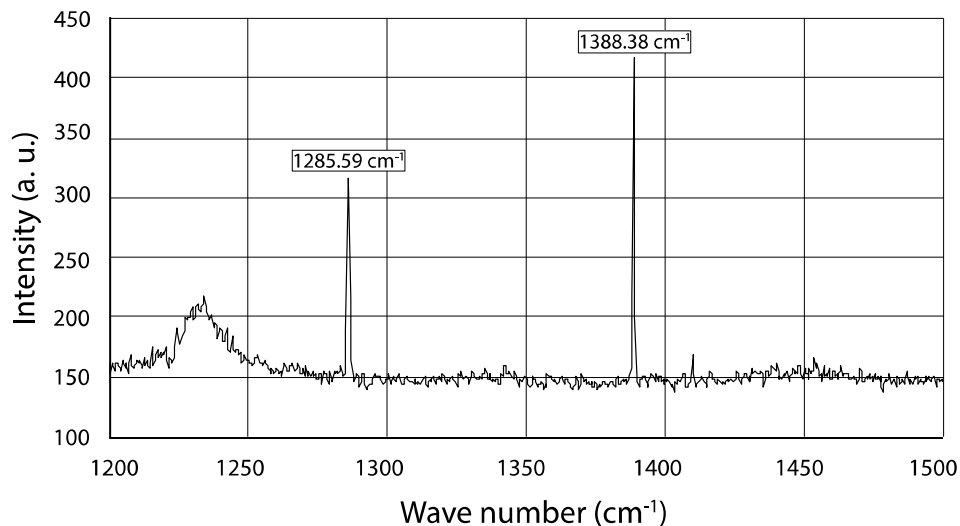
454 Figure 10 – A: Photograph of the thick section from sample GEC 285, where residual pore space and hematite bands are
455 parallel to the quartz bands. B: Optical microscopy photograph of hematite heel shape associated to some fluid inclusion.
456 C: Photograph of a FIA with remarkable CO₂-rich fluid inclusion.

457

458 Three FIAs have been identified and located within the same quartz band (Figure 10A). They are
459 located close to aggregates of hematite laminae. These FIAs are mainly composed of dark single-
460 phase inclusions (Figure 10B, C), interpreted as all-vapour (V) fluid inclusions. Their sizes vary from
461 10 μm to 25 μm, and their shapes are generally regular (oval) and sometimes hexagonal. In the same
462 FIAs single-phase inclusions are also present, much clearer, interpreted as all-liquid (L) fluid
463 inclusions. Very rare two-phase, liquid dominant inclusions are also present, with a Flv of 5 to 20%.
464 As fluid inclusions are not distributed along planes, we can exclude a secondary origin; So these fluid
465 inclusions are contemporaneous with the formation of the quartz band.

466 During cooling down to -130°C, none of the vapour-exclusive fluid inclusions reacted, neither by
467 appearance of solid nor by liquid-vapour phase separation. T_m could be measured in two LV fluid
468 inclusions were -1.1°C and -2.3°C, indicating salinities of 1.9 and 3.8 wt% eq. NaCl respectively. No
469 eutectic temperature could be measured. Data on LV inclusions are too scarce to be representative
470 of fluid properties.

471 Single phase vapour inclusions have been analysed by Raman microspectroscopy using long
472 integration time from 180 s to 600 s. The characteristic signal of CO₂ (Fermi diad bands) has been
473 detected (Figure 11). The majority (75%) of inclusions have revealed the presence of this component.
474 In one case, H₂S has been detected in a dark large (25 μm) fluid inclusion during a very long
475 acquisition time (600 s). Neither CH₄ nor H₂O has been detected. N₂ signal was never higher than
476 that of air, excluding the presence of this gas inside the inclusion. Regarding the few LV fluid
477 inclusions, Raman analyses indicate the vapour phase is composed of CO₂, and the liquid phase of
478 H₂O. Some clear single-phase inclusions have been analysed and show the common H₂O band (3000
479 – 3600 cm⁻¹).



480

481 Figure 11 – CO₂ Raman spectrum obtained in a dark inclusion in sample GEC 285

482

483 An estimation of the density of CO₂ has been obtained by measuring the resonance splitting between
 484 the two peaks of Fermi diad bands (Yamamoto and Kagi, 2006, 2008). This method leads to estimate
 485 a CO₂ density comprised in the interval [0.03 – 0.13] g.cm⁻³. Note that the CO₂ densimeter is
 486 calibrated for density between 0.1 – 1.24 g.cm⁻³, and the interval measured in this study is in the lower
 487 limit of this densimeter. The lack of unmixing during cooling to low temperatures suggests that CO₂
 488 density is probably in the lower part of this range and close to the CO₂ critical density (0.0140 g.cm⁻³;
 489 Angus et al., 1976).

490 Through the calibration of the device according to Dubessy et al. (1989) and Burke (2001) procedure,
 491 the molar fraction of H₂S has been calculated from the area of the spectrum peaks, and was estimated
 492 between 3 and 4 mol%. The presence of CO₂ vapour inclusions on one hand, one-phase water
 493 inclusions on the other hand, and water-CO₂ inclusion furthermore, converges on the idea that the
 494 fluid was a low temperature (< 50°C) mixture of CO₂ and H₂O in an immiscible state.

495

496 **5. Discussion**

497 5.1. Chlorites of Terre-de-Haut: composition and temperature comparison with active
498 geothermal systems.

499 Chlorites are ubiquitous in hydrothermal, metamorphic and diagenetic rocks. Thus, chlorites are
500 found in many geothermal fields of different geological contexts (Browne, 1978). Chlorites found in
501 active geothermal systems at temperature less than or equal to 150°C are not unusual. In fact, chlorite
502 can be formed through a wide range of temperatures, from 70 to 600°C. Different examples from
503 geothermal systems show chlorite formation temperatures below 150°C, as in Cerro-Prieto (Mexico;
504 Reed, 1976) and Los Humeros (Mexico; Martinez-Serrano and Dubois, 1998). Hence, the occurrence
505 of chlorite at this temperature suggests a late apparition, during the cooling of the hydrothermal
506 system.

507

508 *Relevance of the temperature estimates*

509 The quality of chlorite analyses and the homogeneity of these chlorites could be questioned, in
510 particular by the presence of C/S, which would call into question the applicability of thermometers
511 and the temperature estimates. Some facts can be advanced to justify the relevance of the temperature
512 estimates proposed here.

513 (i) *precaution of analysis*. First, and although the XRD data confirms the presence of C/S,
514 microprobe analyses were carried out on crystallites whose petrological and chemical
515 characteristics are those of true chlorite. Second, chemical criteria were applied to exclude
516 analyses which contain significant Ca, Na and K contents.

517 (ii) *a weak influence of residual smectite layers on the temperature calculation*. Even very low Ca,
518 Na and K contents could modify the structural formula calculation. On this point, it can be
519 argued that low-T chlorites usually having a high Si content, often higher 3 apfu (Bourdelle and
520 Cathelineau, 2015), even smectite sheets equivalent to an interlayer charge of 0.1 apfu cannot
521 strongly influence the structural formula calculation (i.e. increasing artificially the Si content),

522 and even less influence the estimate of temperatures. The impact can be quantified around 40°C
523 on temperature estimates, that is not sufficient to consider the thermal difference with
524 Bouillante as no significant (see below).

525 (iii) *the temperature range of C/S*. Even so, the presence of C/S would not call into question the
526 low-T character of the Terre-de-Hauts system: either selected chlorites come from a fluid
527 circulation, and “interlayer cations” are consequently artefacts and temperature estimates are
528 valuable, or the observed chlorites are C/S or the result of an unachieved chloritization of
529 smectite, and the low-T character of the system is supported, since C/S are often observed for
530 $T < 200^{\circ}\text{C}$.

531 (iv) *comparison with other studies*. It can also be noticed that Favier et al. (2021), also analysing
532 chlorites from Terre-de-Haut, presents chlorite compositions with Ca+Na+K contaminations
533 similar to that in the present study, without obtaining temperature estimates as low as those
534 obtained here (see below): residual contaminations do not thus explain the low-T character of
535 our estimates.

536 In consequence, it can be considered that the very low temperatures estimated here from chlorites are
537 valid. Therefore, results from Terre-de-Haut chlorites can be compared with those obtained from
538 other (active or not) geothermal systems related to volcanic arc where chlorite minerals have been
539 characterized, as Guadeloupe (Mas et al., 2006; Verati et al., 2018; Favier et al., 2021), Saint-Martin
540 (Beaufort et al., 1990) and Toyoha (Japan, Inoue et al., 2010).

541

542 *Chlorites from Terre-de-Haut*

543 Petrographic features of chlorite from Terre-de-Haut do not show clear fracture-controlled
544 alteration at microscopic scale, as chlorite is present both as pseudomorphosed minerals and in micro-
545 veins. This feature can lead to imagine a widespread propylitic alteration, located in the “chlorite
546 zone” defined in Beauchamps et al. (2019). However, this propylitic alteration seems located in the

547 most fractured area of Terre-de-Haut. This suggests that fractures, by enhancing fluid circulation,
548 increased the heat input, which then diffused homogeneously through the rock.

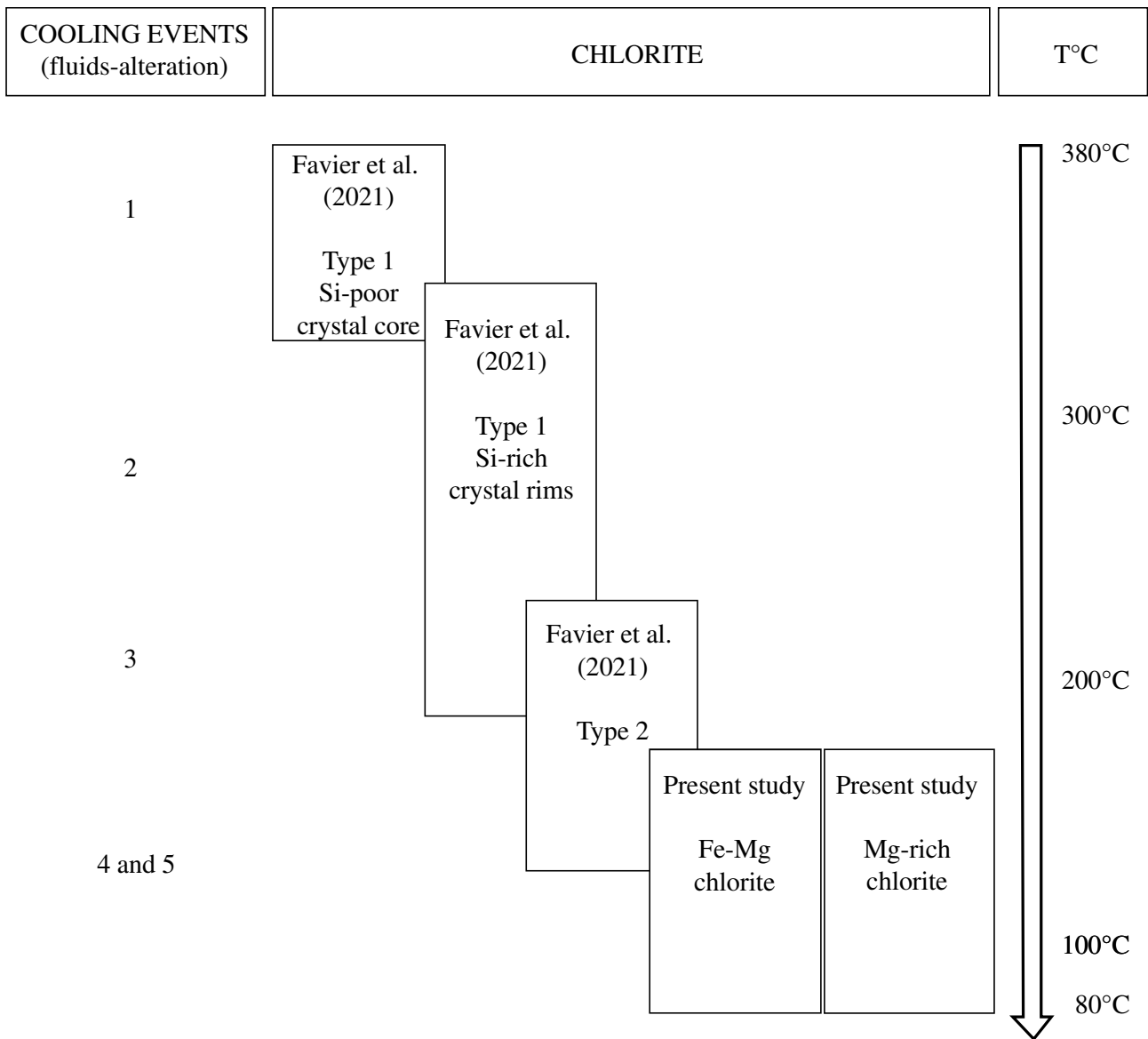
549 The compositional analyses underline the presence of two groups of chlorite, one characterized by a
550 mix Fe-Mg composition (samples GEC 236 and GEC 237) and one by a Mg-rich composition (sample
551 GEC 270), probably resulting from two different fluids. These fluids do not seem to be able to be
552 differentiated by temperature, results of chlorite geothermometry showing that this alteration was
553 achieved at a temperature of about 120°C. In fact, at very low-T as here, the temperature can only be
554 related to the di-tri and Tschermak substitutions, not to the Fe-Mg substitution; the Fe/(Fe+Mg) ratio
555 is sensitive to the fluid and rock composition. In other words, the formation of these two chlorite
556 groups might be from two different fluids with different compositions, but were formed in the same
557 temperature range.

558 Although no other chlorite family has been identified in the present study, the formation of higher
559 temperature chlorite is a hypothesis that must be considered. Favier et al. (2021) performed
560 thermometric study on chlorite from two samples located in north of Grande-Anse beach. Different
561 ranges of temperature are calculated associated to their petrographic features from which two types
562 of chlorites are distinguished:

563 -Type 1 are grey automorphous chemically-zoned crystals associated with muscovite, quartz and
564 epidote, developed at the expense of magmatic pyroxenes, displaying a composition zoning from
565 cores to rims. The Si-poor chemistry of the core leads the author to use Lanari et al. (2014)'s
566 geothermometer which indicates a temperature range of 320-380°C (Figure 12). In contrast, their rims
567 are Si-rich so the Bourdelle et al. (2013)'s geothermometer estimates a formation temperature of 180-
568 350 °C (Figure 12; Favier et al., 2021).

569 -Type 2 are green-grey to yellow fibrous homogeneous Si-rich chlorites associated with fibrous white
570 micas, quartz, calcite, pyrite and/or talc, preferentially located at the rims of pseudomorphosed
571 pyroxenes. Favier et al. (2021) estimate their formation temperatures between 125-230°C by using
572 Bourdelle et al. (2013)'s geothermometer (Figure 12).

573 In contrast to Favier et al. (2021), the present study shows that low formation temperature can be
574 estimated also from the cores of automorphous crystals (type 1), without displaying a temperature
575 zonation within the crystal. This allows highlighting the close link between the nucleation and growth
576 of chlorites and the fluid circulations, in terms of temperature, composition and duration. In our
577 samples, only low temperature chlorites have been observed, with a high homogeneity, which could
578 be explained by the recrystallization/neoformation of these minerals during the final stages of system
579 cooling. The presence of rare epidotes can be considered as a high temperature relic, concordant to
580 the high temperature event described by Favier et al. (2021). No textural relationship between chlorite
581 and these rare epidotes have been observed. In fact, the coexistence in the same samples of HT
582 epidotes with LT chlorites is common in systems which are not totally reequilibrated with the
583 variation of the P-T conditions. The new data from the present study are perfectly compatible with
584 the temperature estimates from Favier et al. (2021), strengthen the hypothesis of a late - low
585 temperature episode. Hence by looking chlorite thermometry a progressive cooling record can be
586 drawn from 380°C to 78°C (Figure 12).



587

588 Figure 12 - Synthesis of thermometric data obtained from the chlorites of Terre-de-Haut. Data are from this study and *Favier et al.*
589 (2021).

590

591 *Chlorites from Guadeloupe*

592 Chlorite has already been studied (i) in the active geothermal system of Bouillante (Mas et al.,
593 2006) and (ii) in Tillet Creek (north of Guadeloupe, in the Basal Complex; Verati et al., 2018; Favier
594 et al., 2019). The latter is not considered as a paleo-geothermal system but corresponds to the oldest
595 volcanic rocks of Guadeloupe 2.8 to 2.7 Ma (Samper et al., 2007) having undergone low-grade
596 hydrothermal metamorphism (Verati et al., 2018).

597 In the Bouillante geothermal system, the chlorite zone corresponds to a pervasive propylitic alteration,
598 considered to be the first alteration stage, at 700 - 900 m depth and a temperature around 250-260°C

599 (Mas et al., 2006). There are some textural differences between chlorites from Bouillante and Terre-
600 de-Haut. Those of Bouillante are located in the porosity of the altered rocks, and made of euhedral
601 crystallites exhibiting a subhexagonal shape with an average width ranging from 2 to 5 μm (Mas et
602 al., 2006), whereas those of Terre-de-Haut and Tillet (Verati et al., 2018) are disseminated within
603 matrix and as pseudomorph of former pyroxenes, with no euhedral shape visible.

604 For comparison, the chemical compositions of Bouillante (Mas et al., 2006), Tillet (Verati et al., 2018;
605 Favier et al., 2019) and Terre-de-Haut chlorites are plotted in a Si-R²⁺ diagram (Figure 13). Chlorites
606 from Bouillante and Tillet are slightly depleted in Si and enriched in Al than those of Terre-de-Haut
607 (Figure 13), i.e. closer to the clinocllore composition. Therefore, the Tschermak and Di-Trioctahedral
608 substitutions are more advanced in Bouillante and Tillet chlorites than in Terre-de-Haut chlorites, that
609 is often an indicator of higher P-T conditions (Bourdelle and Cathelineau, 2015). Using Bourdelle et
610 al. (2013)'s geothermometer applied to chlorite compositions from Mas et al. (2006), estimated
611 temperatures for chlorites in Bouillante are in the range 157-312°C, with a median around 225°C.
612 These estimations are consistent with the temperature range measured in-situ in the well in the chlorite
613 zone (Mas et al., 2006), and higher than temperature estimated for Terre-de-Haut.

614 On the other side, according to Verati et al. (2018) and Favier et al. (2019), chlorites from Tillet Creek
615 return estimated formation temperatures slightly higher than those observed at Bouillante, i.e. 270°C
616 in average as it is shown in Figure 13.

617

618 *Chlorites from Saint-Martin (Lesser Antilles Arc) and Toyoha (Japan)*

619 Similarly to the active system of Bouillante, the paleo-hydrothermal system of Saint-Martin
620 (Lesser Antilles Arc) shows a multi-stage alteration revealed in part by fluid inclusions in quartz and
621 calcite, and additionally by petrographical observations. Hence, three cooling stages have been
622 described, from 510°C to < 50°C (Beaufort et al., 1990, 1992). These chlorites belong to three
623 different assemblages associated to only one alteration event: (i) chlorite + epidote in volcanic and

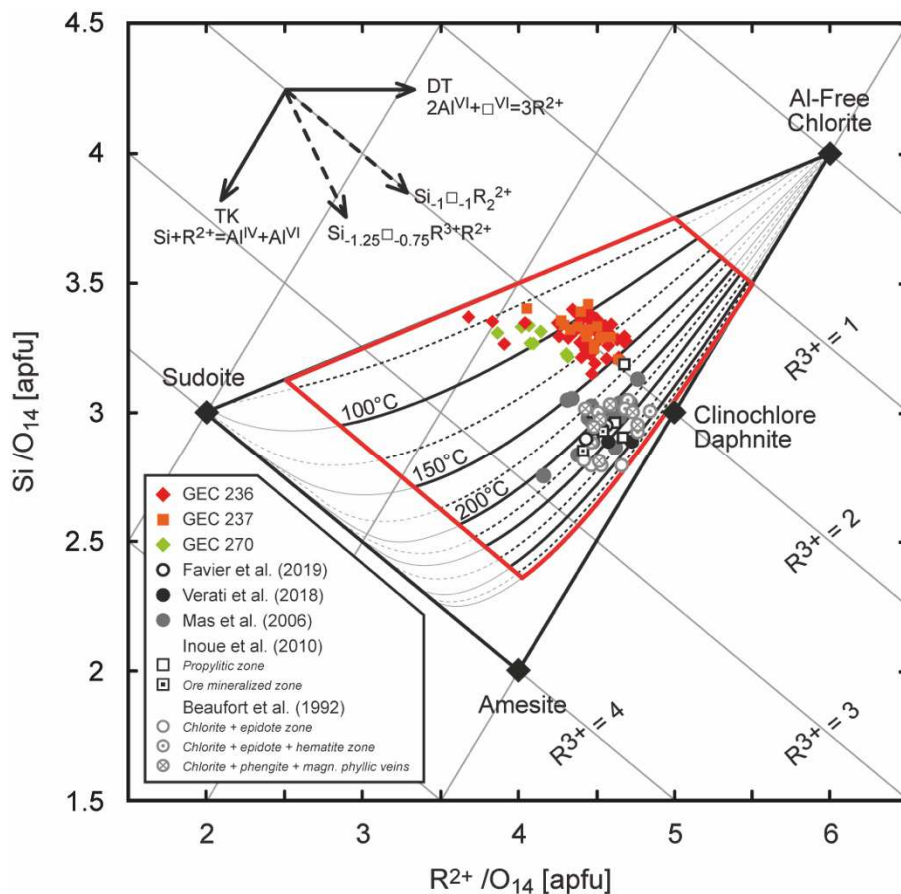
624 sedimentary host rocks; (ii) chlorite + epidote + hematite in volcanic and sedimentary host rocks; (iii)
625 chlorite + phengite ± magnetite in phyllic veins.

626 Data obtained from fluid inclusion analyses in quartz, calcite and baryte lead to an estimated
627 temperature formation between 230 and 300°C for the chlorites co-existing with epidote (Beaufort et
628 al., 1990). These temperatures are consistent with the ones found by using Bourdelle et al. (2013)'s
629 geothermometer (see T-Si-R²⁺ diagram; Figure 13). C/S interstratified minerals (or “swelling
630 chlorite”) have also been observed in the peripheral part of the system (Beaufort et al., 1992). The
631 transition between C/S mixed-layer and chlorite is near 200-220°C. Calcite was associated with C/S
632 and I/S at temperature lower than 200°C (Beaufort et al., 1992).

633

634 In the Toyoha geothermal system (Japan), chlorites have been deeply studied by Inoue et al. (2009,
635 2010). Chlorites from the propylitic zone have been distinguished from chlorites from the ore
636 mineralized zones. For comparison, these chlorite compositions have been plotted in the T-Si-R²⁺
637 diagram (Figure 13). Toyoha chlorites present similar Si and R²⁺ values to the ones of Bouillante and
638 Tillet Creek, except for one chlorite from the propylitic zone. The formation temperature of the
639 chlorite from the two zones are estimated to be within the range of 150-300°C (Inoue et al., 2010),
640 similarly to the one obtained by using Bourdelle et al (2013)'s geothermometer (Figure 13), but it
641 must be emphasized that chlorite from propylitic zone gives similar temperature estimates than the
642 highest temperature chlorite analysed in Terre-de-Haut.

643



644

645 Figure 13 – T-Si-R²⁺ diagram developed by Bourdelle et al. (2015) showing the location of the samples analysed in this
 646 study (in green, orange and red) together with that of chlorite encountered in Bouillante’s geothermal wells (grey dots),
 647 at Tillet Creek (Black dots; 30km north of Bouillante), in Japan (squares) and in Saint-Martin (grey circles).

648

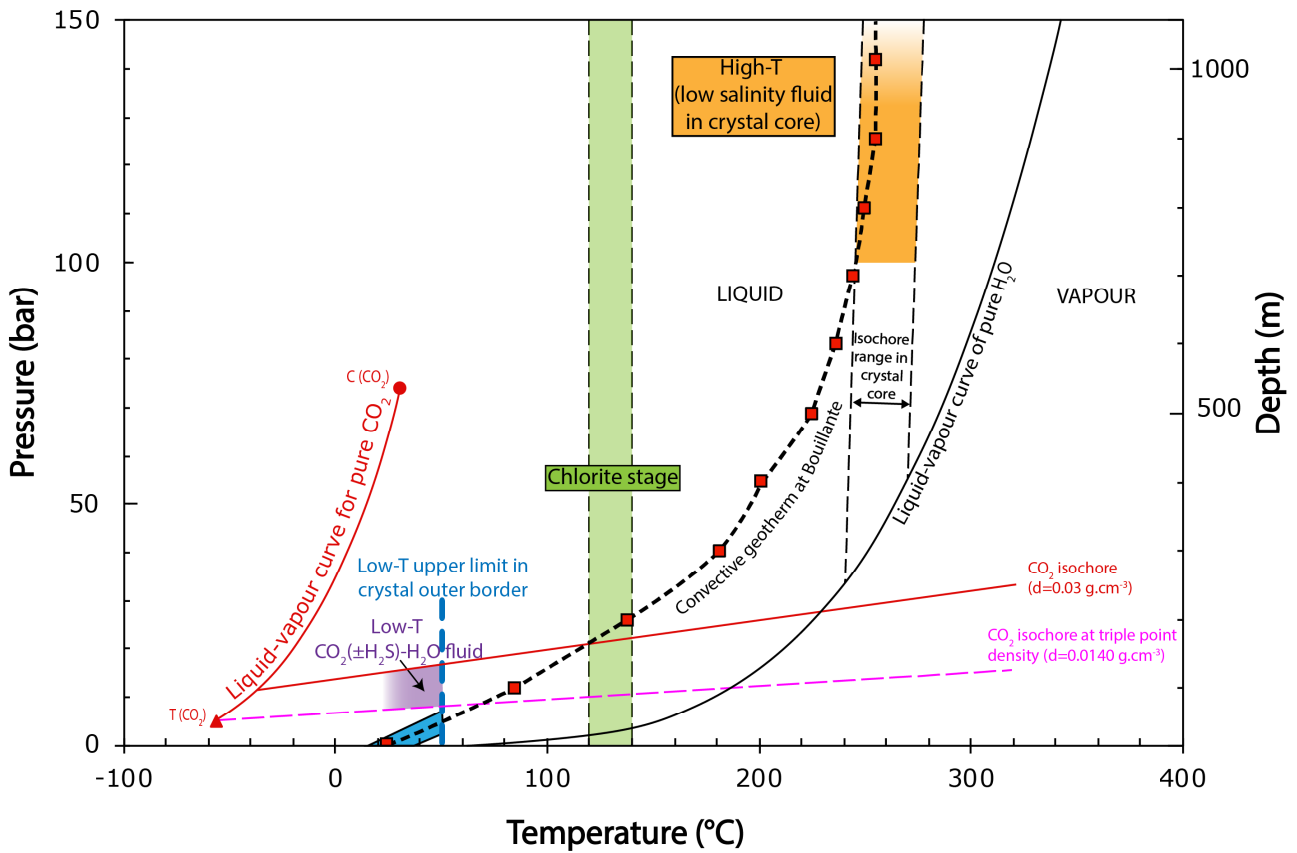
649 Thus, geothermal systems similar to Terre-de-Haut in term of geodynamic context, especially the
 650 Guadeloupean system of Bouillante, often present chlorite formation at higher T than at Terre-de-
 651 Haut. These new data bring certain precision regarding the analogy between the Bouillante
 652 geothermal system and Terre-de-Haut in term of clay mineralogy: their distributions in both sites
 653 show a similar zonation (Beauchamps et al., 2019), but with a chemical contrast of chlorites attesting
 654 to a more advanced cooling stage in the case of Terre-de-Haut.

655

656 5.2. The cooling of the Terre-de-Haut paleo hydrothermal system

657 The thermometric results obtained in this study allow us to develop a general model drawing the
 658 cooling of the hydrothermal system. These results are synthetized in a Pressure-Temperature diagram

659 (Figure 14), where the isochores for the high temperature stage 1 (orange) are calculated with the
 660 model of Zhang and Frantz (1987), and for CO₂ are calculated with the equation of Duan et al. (1995).



661
 662 Figure 14 - Pressure-Temperature diagram summarizing the results of chlorite and fluid inclusions thermometry. The
 663 high-T low salinity fluid corresponds to the second episode of fluid circulation, whereas the low-T fluids to the third
 664 episode. The liquid-vapour curve of H₂O is from Haar et al. (1984), the liquid-vapour curve of CO₂ from Angus et al.
 665 (1976). C (CO₂): critical point of pure CO₂. T (CO₂): triple point of pure CO₂. d: density. The CO₂ isochore 0.03 g.cm⁻³
 666 corresponds to the lowest density estimation using the Raman densimeter; 0.0140 g.cm⁻¹ is the density of the CO₂ triple
 667 point (Angus et al., 1976) . Geotherm at Bouillante measured in well BO6 from Mas et al. (2006).
 668

669 The temperature profile of Bouillante (Traineau et al., 1997; Mas et al., 2006; Bouchot et al., 2010)
 670 has been used to estimate the temperature-pressure path of the Terre-de-Haut fossil hydrothermal
 671 system. The pressure-depth relationship is from data of the well BO-2 (Traineau et al., 2015). This
 672 study of quartz sampled in fractures has shown evidences of fracture-controlled fluid circulation
 673 through two N70 oriented fractures. Three episodes of fluid circulation representing the cooling of
 674 the system can be drawn:

675

676 (1a) A very high temperature episode from 380°C to 180°C. This stage corresponds to the
677 formation of type 1 chlorite described by Favier et al. (2021).

678 (1b) A high temperature episode from 250°C to 115°C conducting to the formation of type 2
679 chlorite described by Favier et al. (2021).

680

681 (2) A high-temperature (240 – 270°C) fluid circulation, deduced from the intersection of the
682 isochores of type 1 inclusions with the temperature profile of the well BO-2, with a probable
683 mixed meteoric and sea-water fluid source (represented by the orange box in Figure 14).
684 Considering the geothermal profile of Bouillante, the fluid pressure was above 100 bar,
685 corresponding to a depth superior to 700 m (Traineau et al., 2015; Figure 14).

686

687 (3a) A low-temperature (<50°C) fluid circulation episode (represented by the blue area in Figure
688 14). Considering the Bouillante thermal profile, the pressure of entrapment can be estimated under
689 8 bars which suggests a very shallow depth of trapping.

690 (3b) Another low-temperature (<50°C) fluid circulation episode (represented by the purple box
691 in Figure 14), associated to a crack and seal functioning (Ramsay, 1980) with antitaxial
692 mechanism (Cox, 1987). These structures suggest a low seismic activity (Jebrak, 1992). The
693 presence of a CO₂-rich fluid, probably as an immiscible phase in water, could have resulted from
694 a fluid acidification with an impact of the redox conditions, associated to hematite precipitation
695 (Kokh et al., 2017). According to the P-T diagram of Figure 14, trapping pressures were between
696 18 and 8 bars by using the density estimations.

697 No relative chronology can be established between the two low-temperature episodes (3a and 3b) as
698 they were recorded in two different structures.

699

700 Based on these observations, it is possible to propose the following scenario:

701 (1) Development of brittle structures oriented N70 which may be due to the reactivation of the fault
702 system corresponding to the valley of La Desirade and to the northern vast scarps bordering this island
703 (Verati et al., 2016).

704 (2) Episode of fluid circulation (1) at high temperature (270-240°C) involving quartz formation in
705 N70 fractures.

706 (3) Diffuse heat transfer with nearly stagnant fluid leading to chlorite formation at 120°C, during the
707 general cooling of the system (as described in Bouillante by Mas et al., 2006).

708 (4) Two low-temperature fluid circulations associated with quartz deposition (< 50°C).

709

710 A different chronology could be that the chlorite episode was the first to appear, associated to a
711 pervasive propylitic alteration as described in Bouillante by Mas et al. (2006). However, the fact that
712 chlorite is found only in the highly-fractured area of North Grande-Anse beach (Beauchamps et al.,
713 2019), might link the crystallization of chlorite to some fracture-controlled fluid circulations.

714

715 Fluid temperature in the active geothermal reservoir of Bouillante is about 250-260°C (Sanjuan et al.,
716 2001; Mas et al, 2006; Guisseau et al, 2007; Bouchot et al, 2010). This temperature corresponds to
717 the temperature estimated for the first fluid circulation event at Terre-de-Haut. However, at
718 Bouillante, the geothermal fluid of around 18-20g/L TDS is interpreted as a mixture of sea water
719 (58%) and fresh water (42%; Sanjuan et al., 2001). In Terre-de-Haut, the very low saline paleo-fluid
720 could be considered being from meteoric origin to a mixture of sea water and fresh water.

721

722 Gas composition has been determined in Bouillante geothermal reservoir, through wells BO-2 and
723 BO-4. Its CO₂ and H₂S content is 95.1 mol% and 2.78 mol% respectively (Sanjuan et al., 2001) which
724 is very similar to the ones estimated in the CO₂ rich fluid-inclusions at Terre-de-Haut. This similitude
725 suggests a similar source, which could be from mixed origin (sedimentary, magmatic) as it is
726 suggested in Bouillante and in the Lesser Antilles Arc by Sanjuan et al. (2001). However, Stimac et

727 al. (2015) shows that gas compositions are sensitive to reservoir rocks, and reservoirs hosted in
728 carbonates or volcanic rocks are usually enriched in CO₂.

729 From an exploration point of view of a potential new geothermal resource located in the south of
730 Basse-Terre, as the tectonic framework of Terre-de-Haut is similar to the one of Basse-Terre (Verati
731 et al., 2016), this study reveals the importance of taking into consideration N70 trending faults as
732 fluid pathway for high temperature geothermal fluid.

733

734 **6. Conclusion**

735 The major interest and complexity of studying a paleo-geothermal system is that the whole
736 hydrothermal history is recorded, from the thermal peak to the death of the geothermal system, thanks
737 to the newly formed hydrothermal minerals and fracturing episodes. In this way, this study brings
738 more precisions to the analogy of the Terre-de-Haut paleo-geothermal system with the Bouillante
739 active geothermal system located 35 km NNW of Terre-de-Haut:

- 740 - First fluid circulation event recorded in the quartz of Terre-de-Haut, at the same temperature as
741 the current deep fluid circulation of Bouillante.
- 742 - Gas composition found in fluid inclusions corresponding to the low-temperature event, similar
743 to the current gas composition of Bouillante.
- 744 - The source of the fluid during the high-temperature fluid circulation event in Terre-de-Haut, is
745 supposed to be of mixed meteoric and sea-water origin, as in Bouillante reservoir.

746 However, some important differences have been highlighted:

- 747 - In Bouillante, no N70 trending structure is known to drive the hydrothermal fluid circulation.
- 748 - Even if the clay mineral sequences are similar, the T conditions of their formation are quite
749 different. Chlorites of Bouillante are chemically different from those observed in Terre-de-Haut,
750 and their formation temperatures are more than 100°C higher than those in Terre-de-Haut.

751

752 These new data allow to better constrain the thermal history of the paleo-geothermal system of Terre-
753 de-Haut, and to distinguish 3 different episodes during the functioning and the cooling of this system,
754 from 270-240°C to below 50°C. The high temperature episode represents the functioning of the
755 geothermal reservoir. The temperature is therefore similar and consistent with the actual geothermal
756 fluid temperature at Bouillante. The low temperature evidences, which have not been identified yet
757 at Bouillante, may represent the end and death of the reservoir, and suggest a change of connectivity
758 to the thermal resource. Hence, these thermometric data demonstrate for the first time the record of
759 the fluid cooling during system evolution in Terre-de-Haut.

760

761 **ACKNOWLEDGMENTS**

762 The discussions and comments of the journal editor, Alessandro Aiuppa, and two anonymous
763 reviewers are gratefully acknowledged.

764 Severine Bellayer (ENS Chimie Lille) is thanked for her help on EMPA handling and Sandra
765 Ventalon (Université de Lille) for her help on fluid inclusion microthermometry and
766 cathodoluminescence handling.

767 This paper is a contribution to the program GEOTREF funded by the French government in the frame
768 of the program "Investissements d'Avenir" and tutored by ADEME.

769 All the participants of GEOTREF project are thanked for their numerous interactions both in the field
770 and in scientific meetings (GéoAzur, GeoRessources, Teranov, KIDOVA, Mines ParisTech, ENS
771 Paris, IMFT, IPGS, LHyGes, UAG, CYU-GEC).

772

773 **REFERENCES**

774 Angus, S., Armstrong, B., & de Reuck, K. M. (Eds.). (1976). Carbon dioxide. Vol. 3 of *International*
775 *Thermodynamic Tables of the Fluid State*. Pergamon Press.

776

777 Beauchamps, G., Ledésert, B., Hébert, R., Navelot, V., & Favier, A. (2019). The characterisation of
778 an exhumed high-temperature paleo-geothermal system on Terre-de-Haut Island (the Les Saintes

779 archipelago, Guadeloupe) in terms of clay minerals and petrophysics. *Geothermal Energy*, 7(1),
780 6.

781

782 Beauducel, F., Antenor-Habazac, C., Bazin, S., De Chabalier, J. B., Nercessian, A., Feuillet, N., ... &
783 Tapponnier, P. (2005). The Mw 6.3 earthquake of Les Saintes (Guadeloupe) on November 21,
784 2004. In *IAVCEI European Seismological Commission Annual Workshop, Saint-Claude*
785 *Guadeloupe, 2005*.

786

787 Beaufort, D., Westercamp, D., Legendre, O., & Meunier, A. (1990). The fossil hydrothermal system
788 of Saint Martin, Lesser Antilles: geology and lateral distribution of alterations. *Journal of*
789 *Volcanology and Geothermal Research*, 40(3), 219-243.

790

791 Beaufort, D., Patrier, P., Meunier, A., & Ottaviani, M. M. (1992). Chemical variations in assemblages
792 including epidote and/or chlorite in the fossil hydrothermal system of Saint Martin (Lesser
793 Antilles). *Journal of Volcanology and Geothermal Research*, 51(1-2), 95-114.

794

795 Bodnar, R. J. (1993). Revised equation and table for determining the freezing point depression of
796 H₂O-NaCl solutions. *Geochimica et Cosmochimica acta*, 57(3), 683-684.

797

798 Bouchot, V., Traineau, H., Guillou-Frottier, L., Thinon, I., Baltassat, J. M., Fabriol, H., ... & Lasne,
799 E. (2010). Assessment of the Bouillante geothermal field (Guadeloupe, French West Indies):
800 toward a conceptual model of the high temperature geothermal system. In *World Geothermal*
801 *Congress 2010*, 8.

802

803 Bourdelle, F., Parra, T., Chopin, C., & Beysac, O. (2013). A new chlorite geothermometer for
804 diagenetic to low-grade metamorphic conditions. *Contributions to Mineralogy and*
805 *Petrology*, 165(4), 723-735.

806

807 Bourdelle, F., & Cathelineau, M. (2015). Low-temperature chlorite geothermometry: a graphical
808 representation based on a T–R₂+–Si diagram. *European Journal of Mineralogy*, 27(5), 617-
809 626.

810

811 Bouysse, P., & Guennoc, P. (1983). Donnees sur la structure de l'arc insulaire des Petites Antilles,
812 entre Ste-Lucie et Anguilla. *Marine Geology*, 53(1-2), 131-166.

813

814 Browne, P. R. L. (1978). Hydrothermal alteration in active geothermal fields. *Annual review of earth*
815 *and planetary sciences*, 6(1), 229-248.

816

817 Burke, E. A. (2001). Raman microspectrometry of fluid inclusions. *Lithos*, 55(1-4), 139-158.

818

819 DeMets, C., Jansma, P. E., Mattioli, G. S., Dixon, T. H., Farina, F., Bilham, R., ... & Mann, P. (2000).
820 GPS geodetic constraints on Caribbean-North America plate motion. *Geophysical Research*
821 *Letters*, 27(3), 437-440.

822

823 Diamond L.W. (2003) CHAPTER 5. INTRODUCTION TO GAS-BEARING, AQUEOUS FLUID
824 INCLUSIONS. In: Fluid Inclusions: Analysis and Interpretation (I. Samson, A. Anderson, D.
825 Marshall, Eds.), *Mineralogical Association of Canada Short Course Series*, (32), 101-158.

826

827 Duan, Z., Møller, N., & Weare, J. H. (1995). Equation of state for the NaCl-H₂O-CO₂ system:
828 prediction of phase equilibria and volumetric properties. *Geochimica et Cosmochimica*
829 *Acta*, 59(14), 2869-2882.

830

831 Dubessy, J., Poty, B., & Ramboz, C. (1989). Advances in COHNS fluid geochemistry based on
832 micro-Raman spectrometric analysis of fluid inclusions. *European journal of Mineralogy*, 1(4),
833 517-534.

834

835 Favier, A., Lardeaux, J. M., Corsini, M., Verati, C., Navelot, V., Géraud, Y., ... & Voitus, E. (2021).
836 Characterization of an exhumed high-temperature hydrothermal system and its application for
837 deep geothermal exploration: An example from Terre-de-Haut Island (Guadeloupe archipelago,
838 Lesser Antilles volcanic arc). *Journal of Volcanology and Geothermal Research*, 107256.

839

840 Goldstein, R.H. & Reynolds, T.J. (1994): Systematics of fluid inclusions in diagenetic minerals.
841 SEPM Short Course 31. *Society for Sedimentary Geology*, 199.

842

843 Guisseau, D., Mas, P. P., Beaufort, D., Girard, J. P., Inoue, A., Sanjuan, B., ... & Genter, A. (2007).
844 Significance of the depth-related transition montmorillonite-beidellite in the Bouillante
845 geothermal field (Guadeloupe, Lesser Antilles). *American Mineralogist*, 92(11-12), 1800-1813.

846

847 Hawkesworth, C. J., & Powell, M. (1980). Magma genesis in the Lesser Antilles island arc. *Earth*
848 *and Planetary Science Letters*, 51(2), 297-308.

849

850 Holtzapffel, T. (1985). Preparation, XRD analysis and determination. *Annals of the Geological*
851 *Society of the Northern. Clay Miner*, 12, 136.

852

853 Inoue, A., Meunier, A., Patrier-Mas, P., Rigault, C., Beaufort, D., & Vieillard, P. (2009). Application
854 of chemical geothermometry to low-temperature trioctahedral chlorites. *Clays and Clay*
855 *Minerals*, 57(3), 371-382.

856

857 Inoue, A., Kurokawa, K., & Hatta, T. (2010). Application of chlorite geothermometry to
858 hydrothermal alteration in Toyoha geothermal system, southwestern Hokkaido, Japan. *Resource*
859 *Geology*, 60(1), 52-70.

860

861 Jacques, D., & Maury, R. (1988a). Carte géologique à 1/20000, département de la Guadeloupe.
862 *BRGM, Service Géologique Nationale, Orléans.*

863

864 Jacques, D., & Maury, R. (1988b). L'archipel des Saintes (Guadeloupe, Petites Antilles) : géologie
865 et pétrologie. *Géol. Fr.* 11(2-3), 89-99.

866

867 Jacques, D., Maury, R. C., & Bellon, H. (1984). Géologie et géochronologie ^{40}K - ^{40}Ar des îles des
868 Saintes (Guadeloupe). *Comptes-rendus des séances de l'Académie des sciences. Série 2,*
869 *Mécanique-physique, chimie, sciences de l'univers, sciences de la terre*, 299(11), 721-726.

870

871 Javey, C., Alsac, C., & Mervoyer, B. (1974). Le volcanisme des Saintes. *Livret-Guide Excursions*
872 *A, 6*, 65-76.

873

874 Jébrak, M. (1992). Les textures intra-filoniennes, marqueurs des conditions hydrauliques et
875 tectoniques. *Chronique de la Recherche Minière*, 506, 25-35.

876

877 Kokh, M. A., Akinfiev, N. N., Pokrovski, G. S., Salvi, S., & Guillaume, D. (2017). The role of carbon
878 dioxide in the transport and fractionation of metals by geological fluids. *Geochimica et*
879 *Cosmochimica Acta*, 197, 433-466.

880

881 Lanari, P., Wagner, T., & Vidal, O. (2014). A thermodynamic model for di-trioctahedral chlorite from
882 experimental and natural data in the system MgO–FeO–Al₂O₃–SiO₂–H₂O: applications to
883 P–T sections and geothermometry. *Contributions to Mineralogy and Petrology*, 167(2), 968.

884

885 Martinez-Serrano, R. G., & Dubois, M. (1998). Chemical variations in chlorite at the Los Humeros
886 geothermal system, Mexico. *Clays and clay minerals*, 46(6), 615-628.

887

888 Mas, A., Guisseau, D., Mas, P. P., Beaufort, D., Genter, A., Sanjuan, B., & Girard, J. P. (2006). Clay
889 minerals related to the hydrothermal activity of the Bouillante geothermal field (Guadeloupe).
890 *Journal of Volcanology and Geothermal Research*, 158(3), 380-400.

891

892 Navelot, V., Géraud, Y., Favier, A., Diraison, M., Corsini, M., Lardeaux, J. M., ... & Beauchamps,
893 G. (2018). Petrophysical properties of volcanic rocks and impacts of hydrothermal alteration in
894 the Guadeloupe Archipelago (West Indies). *Journal of Volcanology and Geothermal*
895 *Research*, 360, 1-21.

896

897 Ramsay, J. G. (1980). The crack–seal mechanism of rock deformation. *Nature*, 284(5752), 135.

898

899 Reed, M. J. (1976). Geology and hydrothermal metamorphism in the Cerro Prieto geothermal field,
900 Mexico. In *2nd UN symposium on the development and use of geothermal resources*, 1, 539-547.

901

902 Roedder, E. (1984). Volume 12: Fluid inclusions. *Reviews in mineralogy*, 12.

903

904 Samper, A., Quidelleur, X., Lahitte, P., & Mollex, D. (2007). Timing of effusive volcanism and
905 collapse events within an oceanic arc island: Basse-Terre, Guadeloupe archipelago (Lesser
906 Antilles Arc). *Earth and Planetary Science Letters*, 258(1), 175-191.

907

908 Sanjuan, B., Brach, M., & Lasne, E. (2001). Bouillante geothermal field: mixing and water/rock
909 interaction processes at 250° C. *Water Rock Interaction, WRI-10, International Symposium on*
910 *Water Rock Interaction, Jun 2001, Villasimius, Italy*, 911-914.

911

912 Stimac, J., Goff, F., & Goff, C. J. (2015). Intrusion-related geothermal systems. In *The Encyclopedia*
913 *of Volcanoes*, Academic Press., 799-822.

914

915 Symithe, S., Calais, E., De Chabalier, J. B., Robertson, R., & Higgins, M. (2015). Current block
916 motions and strain accumulation on active faults in the Caribbean. *Journal of Geophysical*
917 *Research: Solid Earth*, 120(5), 3748-3774.

918

919 Traineau, H., Sanjuan, B., Beaufort, D., Brach, M., Castaing, C., Correia, H., ... & Herbrich, B.
920 (1997). The Bouillante geothermal field (FWI) revisited: new data on the fractured geothermal
921 reservoir in light of a future stimulation experiment in a low productive well. In *Proc 22nd*
922 *Workshop on Geothermal Reservoir Engineering, Stanford University, SGP-TR-155*.

923

924 Traineau, H., Sanjuan, B., & Lasne, E. (2015). Main results of a long-term monitoring of the
925 Bouillante geothermal reservoir during its exploitation. In *Proceedings of World Geothermal*
926 *Congress*.

927

- 928 Verati, C., Mazabraud, Y., Lardeaux, J. M., Corsini, M., Schneider, D., Voitus, E., & Zami, F. (2016).
929 Tectonic evolution of Les Saintes archipelago (Guadeloupe, French West Indies): relation with
930 the Lesser Antilles arc system. *Bulletin de la Société géologique de France*, 187(1), 3-10.
931
- 932 Verati, C., Lardeaux, J. M., Favier, A., Corsini, M., Philippon, M., & Legendre, L. (2018). Arc-related
933 metamorphism in the Guadeloupe archipelago (Lesser Antilles active island arc): First report and
934 consequences. *Lithos*, 320, 592-598.
935
- 936 Yamamoto, J., & Kagi, H. (2006). Extended micro-Raman densimeter for CO₂ applicable to mantle-
937 originated fluid inclusions. *Chemistry Letters*, 35(6), 610-611.
938
- 939 Yamamoto, J., & Kagi, H. (2008). Application of densimetry using micro-Raman spectroscopy for
940 CO₂ fluid inclusions: a probe for elastic strengths of mantle minerals. *European Journal of*
941 *Mineralogy*, 20(4), 529-535.
942
- 943 Zami, F., Quidelleur, X., Ricci, J., Lebrun, J. F., & Samper, A. (2014). Initial sub-aerial volcanic
944 activity along the central Lesser Antilles inner arc: New K–Ar ages from Les Saintes
945 volcanoes. *Journal of Volcanology and Geothermal Research*, 287, 12-21.
946
- 947 Zhang, Y. G., & Frantz, J. D. (1987). Determination of the homogenization temperatures and densities
948 of supercritical fluids in the system NaClKClCaCl₂H₂O using synthetic fluid
949 inclusions. *Chemical Geology*, 64(3-4), 335-350.
950